# Microtubule-based nucleation results in a large sensitivity to cell geometry of the plant cortical array

Marco Saltini[1], Eva E. Deinum[1,*]

[1]: Mathematical & Statistical Methods (Biometris), Plant Science Group, Wageningen University, 6708 PB Wageningen, The Netherlands

[*]: Corresponding author: eva.deinumwur.nl

*Keywords*: plant cortical microtubules, nucleation, array orientation, biophysical modelling, CorticalSim, computational biology.

**Abstract**

Many plant cell functions, including cell morphogenesis and anisotropic growth, rely on the self-organisation of cortical microtubules into aligned arrays with the correct orientation. An important ongoing debate is how cell geometry, wall mechanical stresses, and other internal and external cues are integrated to determine the orientation of the cortical array. Here, we demonstrate that microtubule-based nucleation can markedly shift the balance between these often competing forces. For this, we developed a novel, more realistic model for microtubule-based nucleation in the simulation platform CorticalSim, which avoids the longstanding inhomogeneity problem stemming from previous, less realistic models for microtubule-based nucleation. We show that microtubule-based nucleation increases the sensitivity of the array to cell geometry, extending the regime of spontaneous alignment compared to isotropic nucleation. In the case of cylindrical cell shapes, we show that this translates in a strong tendency to align in the transverse direction rather than along the vertical axis, and this is robust against small directional cues in the longitudinal direction. Our model provides a powerful tool for investigating how plant cells integrate multiple biases to orient their cortical arrays, offering new insights into the biophysical mechanisms underlying cell shape and growth.

## Introduction

Plants take their shape through coordinated processes of cell division, expansion and differentiation. At the cellular level, many of these processes are shaped by the plant cortical microtubule array [1–3]. This dynamic structure of membrane associated microtubules guides the anisotropic deposition of cellulose microfibrils, the main load bearing component of the cell wall, and predicts the future cell division site [4–7]. Under the right conditions [8, 9], these dynamic microtubules can self-organise into a highly aligned array. This self-organisation depends on frequent collisional interactions among microtubules, resulting in angle-dependent outcomes [10]. The dynamics of individual microtubules, by controlling the strength of such collisional interactions, play a crucial role in this organisation [8,11]. Microtubule nucleation, particularly the orientation of newly-generated microtubules in relation to their parent microtubules (Figure 1AB), has a profound impact on the self-organisation of the cortical microtubule array and its ability to adopt complex patterns [12–17]. Consequently, any quantitative predictions from computer simulations critically depend on a sufficiently realistic implementation of microtubule nucleation.

This is particularly relevant in the ongoing debate about what controls the orientation of the cortical microtubule array (Figure 1C), which is the focus of this manuscript. Array orientation is significantly influenced by a combination of global and local cues. For example, global cues such as cell geometry can favour array orientation along the shortest closed circumferences of the cell [18,19]. Local cues, including the alignment of microtubules with mechanical stresses [20], could select for a specific orientation among these, or potentially even override the global cues [21, 22]. Given that new microtubules in plants typically nucleate in directions strongly correlated with the orientation of their parent microtubule [16, 17, 23], how microtubules are nucleated in simulations of the cortical array is crucial. Indeed, different nucleation modes result in different sensitivities to local and global cues [12, 13, 24, 25]. It is hypothesized that the basis of this different behaviour is that microtubule based nucleation increases bundle life time and, thereby, longer maintains the information stored in the constituent microtubules [16, 24]. Therefore, the ability to realistically simulate microtubule nucleation is critical for any computational study that involves a competition between local and global cues affecting alignment and orientation.

Explicit stochastic simulations (Figure 1D-F) have a long tradition in the study of cortical array behaviour (e.g., see [9, 24] for reviews). Despite the importance of microtubule-based nucleation, however, most computational and theoretical research on microtubule arrays has traditionally employed isotropic nucleation, where microtubules are initiated at random positions with random orientations. While helpful for understanding the effects of microtubule collisions [8, 10, 26] and geometrical constraints on alignment [18, 21, 27–29], this approach ignores that microtubules often nucleate from existing ones [15,23,30,31]. Many simulation studies with microtubule-based nucleation [13, 16, 32, 33], however, suffer from a so-called "inhomogeneity problem" [12]. In essence, this is a computational problem arising from a naive implementation of microtubule-based nucleation, i.e., when the local share of microtubule-based nucleation is linearly dependent on the local density. This density-dependence causes a positive feedback on local microtubule density, leading to overly dense regions and very sparse areas in between. As cellulose synthase complexes are preferentially inserted near microtubules [6], such inhomogeneities would lead to structural weaknesses in the cell wall. While this feedback loop originates from the biological reality of microbule-based nucleation, the naive implementation has no force counteracting the positive feedback. In reality, however, the local nucleation rate saturates with density, thereby ensuring homogeneity [12].

Jacobs et al. [12] showed that one solution to this problem is to explicitly consider the appearance

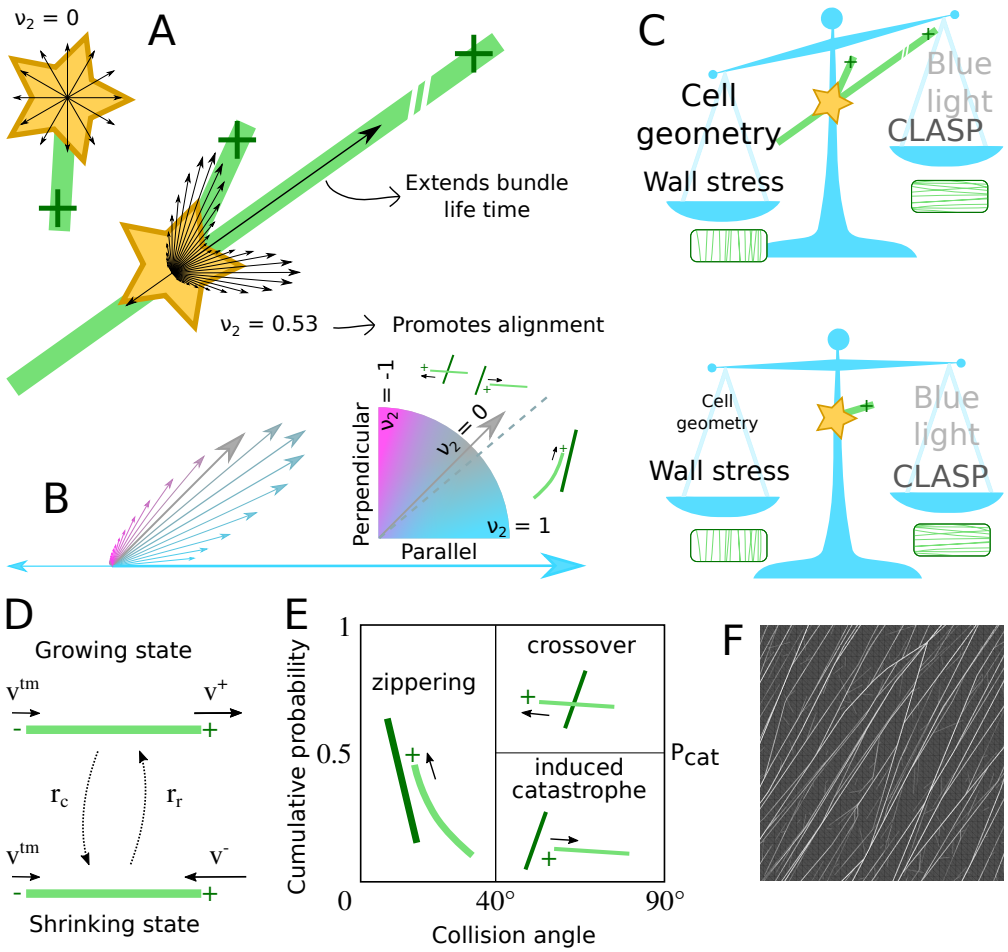


Figure 1: **Different nucleation modes (and their hypothetical impact)**. (A) Unbound nucleation typically has a uniformly distributed orientation, whereas microtubule-based nucleation follows a specific distribution relative to the parent microtubule, with parallel, antiparallel and "branched" components. The part parallel to the parent microtubule (31% in our simulations [16]) can increase the life time of a microtubule bundle. Additionally, the distribution of nucleation angles is overall co-aligned with the parent microtubule, which increases the parameter regime of spontaneous microtubule alignment. (B) Different components of the nucleation angle distribution coloured by their degree of co-alignment (contribution ($\sim \cos(2\theta)$) to $\nu_2$, the second Fourier coefficient.) An angle of 45° is neutral in this respect, indicated by the bold grey arrow. The dashed line indicates the (40°) boundary between zippering and other outcomes (see panel E) if the nascent microtubule would collide into another microtubule with the same orientation as its parent. (C) As a consequence of the properties of microtubule based nucleation, the persistence of bundles increases, which allows for longer retention and further communication of the information about the array stored in that bundle. This renders the array as a whole more sensitive to global cues like the size and shape (geometry) of the cell. The strength of different cues can vary, as visualized by different shades of grey. (D-F) **Overview of model dynamics**. (D) Dynamics of individual microtubules. The plus-end (+) stochastically switches between the growing and shrinking state, whereas the minus-end (-) shows steady retraction. (E) Angle dependent collision outcomes. (F) Fragment of an example simulated array. Individual microtubules are drawn with a degree of transparency, so thicker bundles appear as stronger white lines.

and diffusion at the membrane of nucleation complexes. They implemented this in a simplified array simulation framework dubbed CorticalSimple, in which alignment of microtubules is taken for granted, i.e., they all have an exactly transverse orientation [12]. In CorticalSimple, nucleation complex diffusion takes up a large fraction of the computational time, even though nucleation itself is a relatively rare event. The diffusion of explicit nucleation complexes is also employed in CytoSim (e.g., [34]), in which the computational cost of diffusing "nucleators" is less problematic, because the microtubule model itself is computationally much more demanding due to its larger degree of mechanical realism. The computational load of CytoSim, however, makes it less suitable for simulating a large number of instances of plant cortical arrays, as would be required for quantitatively investigating the subtle forces acting on array orientation. A different platform, CorticalSim, is specifically developed for high speed. Previous publications with CorticalSim heavily use its computational efficiency, which allows for accurate computation of ensemble statistics from many simulations combined with exploration of parameter space in relatively short time [5,11,13,16,18,35]. Such efficiency not only allows for more robust conclusions, but also enables the investigation of different types of questions. The computational efficiency of CorticalSim stems from its adoption of an event-driven approach for microtubule dynamics and interaction, which updates the system following each event rather than at fixed time intervals [11,19]. To maintain the computational advantages of CorticalSim we, therefore, developed a new nucleation algorithm that efficiently approximates the diffusion of nucleation complexes. Our approach increases the biological realism of microtubule-based nucleation, enabling the natural emergence of density-dependence from the nucleation process at both local and global scales, and overcomes the long-standing issue of inhomogeneity. Furthermore, it maintains the computational efficiency of CorticalSim.

By comparing arrays produced by our new microtubule-based algorithm with those generated through isotropic and previous global density-dependent nucleation modes, we show that cell geometry has a much stronger impact on array orientation than previously thought. By developing this more realistic microtubule-based nucleation, we also identified a major artefact in the behaviour of previous simulated arrays: not the possibilities for forming a single closed and relatively short path around a geometry, but minimizing the degree of conflict in the entire array determines the preferred orientation(s) on a given geometry. More in general, our results show that different nucleation modes have major impacts in the responsiveness of the array to cues of different types. These findings have important consequences for our understanding of array orientation and beyond.

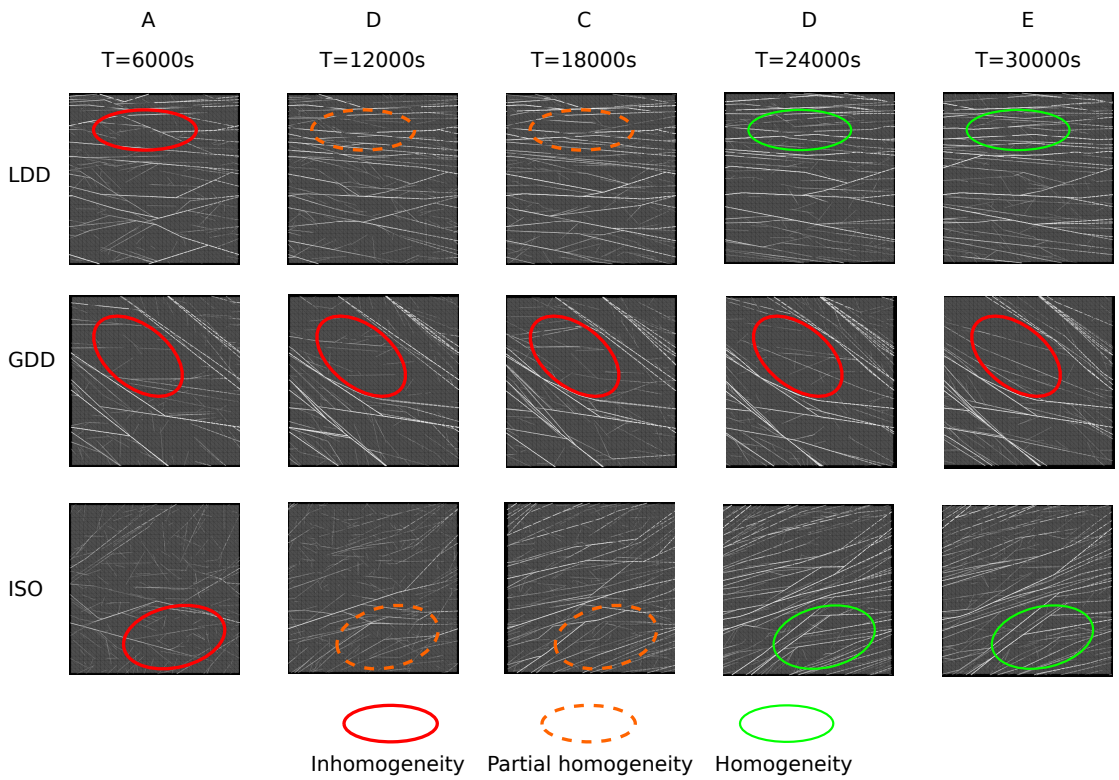


Figure 2: **Simulation snapshots show that the new LDD microtubule-based nucleation yields much more homogeneous arrays than old GDD microtubule-based nucleation**. Simulation snapshots of a $40 \times 40\mu$m square domain taken every 6000 s (100 min). Red thick oval represent areas of inhomogeneity, orange dashed ovals areas of partial homogeneity, and green thin ovals areas where the array is homogeneous. Note the persistence of areas of inhomogeneity in the GDD case, compared to the transient inhomogeneity in the LDD and ISO cases. In these simulations, catastrophe rates values correspond to data points marked with large symbols in Figure 3, i.e., (LDD) $r_c = 0.00275$ s$^{-1}$, (GDD) $r_c = 0.003$ s$^{-1}$, (ISO) $r_c = 0.002$ s$^{-1}$.

# 1 Results

## 1.1 Microtubule based nucleation supports homogeneous arrays

The hypothesis that microtubule based nucleation improves alignment of the cortical array through extending bundle life time [16] is critical to understanding the impact of this type of nucleation. Previously published results, however, all depended on algorithms that introduce a global competition for nucleation (global density-dependence (GDD) in our study), so it cannot be ruled out that this conclusion was based on artefacts, i.e., the inhomogeneity problem introduced by this algorithm. We, therefore, verified that our improved algorithm (LDD for local density-dependence) produces homogeneous arrays. Figure 2 shows that LDD indeed produced homogeneous arrays with default parameters (Table 1), comparable to isotropic nucleation (ISO), whereas the old GDD resulted in large inhomogeneities, visible as a combination of both large, nearly empty areas and a few very dense bundles. With LDD and ISO, inhomogeneities in the early array disappeared over time,

whereas with GDD, array inhomogeneity increased with time (Figure 2).

### 1.2 Microtubule based nucleation stimulates array alignment

Although with LDD the visual appearance was rather similar to arrays produced with isotropic nucleation, LDD microtubule-based nucleation increased the parameter regime for spontaneous alignment almost as much as the old GDD algorithm (Figure 3A). In this figure, the parameters describing the dynamic instability of individual microtubules and the nucleation rate are collapsed onto a single number $G$, defined in Equation (8). This so-called control parameter is the (negative) ratio of two length scales: an interaction length and the average microtubule length without interactions. As $G$ increases towards zero, the average number of interactions per microtubule life time increases. With sufficient interactions, spontaneous alignment occurs (order parameter $S_2$ (Equation (6)) on the vertical axis increases from near zero to near one). With this understanding of the process [8, 9, 19, 24], the result in Figure 3A can be restated as follows: microtubule-based nucleation roughly halves the minimal number of interactions per average microtubule life time that is required for spontaneous alignment.

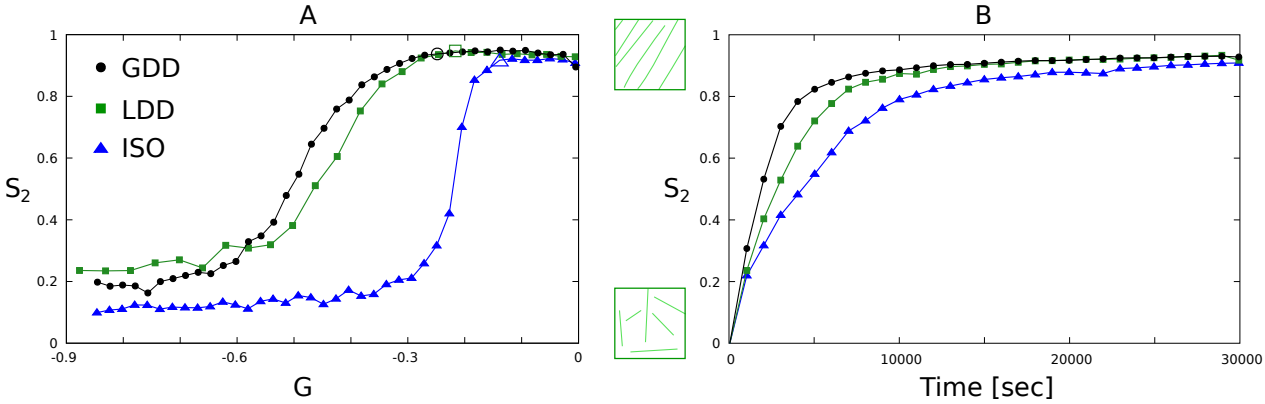


Figure 3: **LDD nucleation maintains the alignment promoting effect of microtubule-based nucleation** as previously reported for GDD. Aligned regime for LDD, GDD, and ISO nucleation modes on a $40\times40$ $\mu$m$^2$ square periodic geometry. (A) Median over 100 independent simulation runs of the order parameter $S_2$ as function of the control parameter $G$ at $T = 3 \times 10^4$ s (8 h, 20 min). Data points marked as larger, empty circle, square, or triangle correspond to the parameter values used for panel (B). (B) Median over 100 independent simulation runs of the order parameter $S_2$ as function of the simulation time for selected values of $G$ (data points marked with large symbols in panel (A)) in the ordered regime. Error bars of (A) can be found in Figure S1.

Alignment also occurred faster with microtubule-based than with isotropic nucleation, when comparing parameters at similar points in the $S_2(G)$-curve (Figure 3B). In this case, the relative order of the nucleation algorithms was the same, with fastest alignment with GDD. The relative differences between LDD and the other algorithms, however, had changed. The larger difference between LDD and GDD most likely resulted from the improved realism of the LDD algorithm: LDD incorporates the experimental observation that nucleation complexes nucleate with higher rate when they are attached to microtubules [13, 15], whereas GDD uses the same rate for bound and unbound complexes. Consequently, the initial nucleation rate is reduced with LDD, but not with

the other algorithms. For a treatment of the early nucleation rate, we refer to [12]. So, microtubule based nucleation speeds up alignment even when the initial nucleation rate is reduced (but see [**?**]).

Verification simulations with LDD show how the fraction of microtubule based nucleation increases with increasing microtubule density and the nucleation rate increases to equilibrium levels (Figure S4). At a high density around 5 $\mu$m$^{-1}$, the fraction microtubule based nucleation was somewhat lower than reported before (95% when using local density, Figure S4, compared to 98% in [15]), which can likely be explained by the fact that, here, we do not take into account that the appearance of nucleation complexes at the membrane is biased towards existing microtubules [12, 15]. As expected, the relation between microtubule density and fraction of microtubule based nucleation was tighter when using the local microtubule concentration than the global one.

Together, these results validate the conclusion that microtubule-based nucleation promotes alignment. Note that this will still depend on the distribution of nucleation angles relative to the parent microtubule (see [16, 17]), which is experimentally observed to be (moderately) co-aligned with the parent microtubule [15, 23].

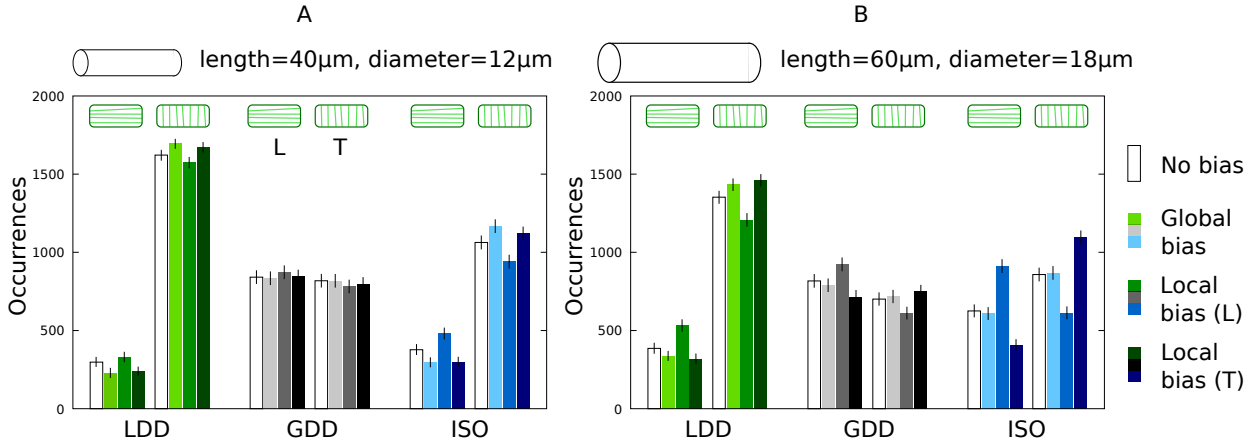


Figure 4: **LDD microtubule-based nucleation increases the sensitivity of array orientation to cell geometry**. Number of aligned arrays at $T = 3 \times 10^4$ s (8 h, 20 min) with a transverse (T; when $-10° < \Theta_2 < 10°$), or longitudinal (L; when $80° < \Theta_2 < 100°$) orientation, with or without directional biases: 8% increase in catastrophe rate at the cylinder caps for the global bias, and 8% increase in maximum rescue rate according to Equation (10) for the local bias. The simulation domain is a cylinder of (A) 40$\mu$m length and 12$\mu$m diameter, and (B) 60$\mu$m length and 18$\mu$m diameter. Error bars represent 95% confidence interval according to a binomial model (computed using the binom.test function in R statistical package version 3.6.3). In these simulations, $r_c = 0.00225$ s$^{-1}$.

### 1.3 Microtubule-based nucleation increases sensititivity to geometrical cues

The consequence of increased microtubule bundle lifetime is that the information about the array stored in the bundle is maintained longer. Microtubule-based nucleation could moreover facilitate increased bundle length, which allows information to propagate further through the array. Both processes could change the sensitivity of the array to geometric cues and shift the balance between different types of cues (Figure 1C). This would have major implications for the ongoing debate on what determines the orientation of the cortical array [5, 24, 28, 36, 37]. We, therefore, investigated

the preferred orientation of simulated arrays with the three nucleation algorithms on cylindrical cells. Figure 4 shows that with LDD microtubule-based and isotropic nucleation, the cylindrical geometry favoured a transverse orientation over a longitudinal one. This effect was stronger for microtubule-based nucleation than for isotropic. GDD, however, behaved in such a different way, that we suspect this behaviour may be caused by an artefact. We, therefore, first focus on the comparison of LDD and isotropic and investigate the deviating GDD-behaviour in more detail later on.

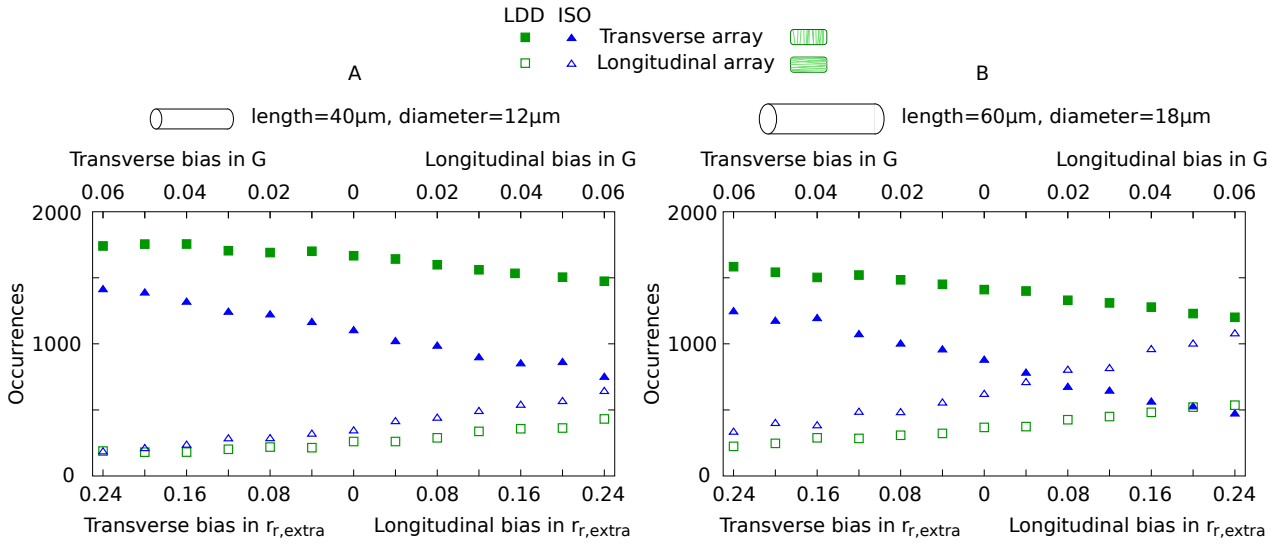


Figure 5: **Large orientational biases are required to reliably control array orientation on cylindrical cells.** Number of aligned arrays at $T = 3 \times 10^4$ s (8 h, 20 min) with a transverse (filled symbols) or longitudinal (empty symbols) orientation for the LDD (green squares) and ISO (blue triangles) cases, for different values of the longitudinal bias in $r_{r,\text{extra}}$ according to Equation (10). The simulation domain is a cylinder of (A) 40$\mu$m length and 12$\mu$m diameter, and (B) 60$\mu$m length and 18$\mu$m diameter. The upper horizontal axis translates the increased rescue rate into the maximum increase in $G$ in the favoured direction. Error bars have been omitted because they are approximately the same size as the symbols. Similar graphs including GDD nucleation can be found in Figure S10. In these simulations, $r_c = 0.00225$ s$^{-1}$.

On larger cells, information must travel further to ensure whole cell coordination of the array orientation. Consequently, obtaining a consistent orientation should be harder on larger domains. Comparing periodic square domains of increasing sizes, we indeed observed a consistent decrease in the median $S_2$-value in the aligned regime for all nucleation modes, both in $G, S_2$-curves (Figure S5) and in ($S_2$, density) scatter plots (Figure S6). This effect was strongest with isotropic nucleation. Snapshots of individual simulations on $80 \times 80$ $\mu m^2$ periodic squares in the aligned regime show that multiple highly aligned domains with different orientations can form (Figure 6), leading to a reduction of the (global) $S_2$. The ($S_2$, density) scatter plots (Figure S6) show that this phenomenon occurred most often and most extreme with isotropic nucleation, with some points with high density and high $G$ (i.e., well inside the aligned regime) having (global) $S_2$ values typical of disordered arrays.

Along the same lines, we observed that geometry had a weaker effect on array orientation on the

larger cells (Figure 4B). Also the impact of a higher catastrophe rate at the cylinder caps ("global bias: an 8% increase of $r_c$) was weaker on the larger cells. The impact of local cues ("local bias", an 8% increase of rescue rate $r_r$ in the indicated direction), on the other hand, was stronger on the larger cells. Consistent with the above considerations about bundle lifetime and information propagation, the sensitivity to global cues (geometry itself and "global bias") was larger for LDD microtubule-based nucleation and the sensitivity to local cues was larger with isotropic nucleation.

As an 8% increase in $r_r$ for the local bias only resulted in a 2% increase in $G$, we varied the strength of the local bias over a larger range (Figure 5). Isotropic nucleation was again more sensitive to changes in the local bias. Still, even with isotropic nucleation, the largest bias tested towards longitudinal still resulted in a small majority of transverse arrays on the small cylinders (maximum 24% increase of $r_r$, corresponding to a 6% increase of $G$ for perfectly longitudinal microtubules). These results show that the impact of geometry itself is substantial even with isotropic nucleation. Microtubule-based nucleation further increases this impact.

### 1.3.1 High sensitivity to short closed paths is an artefact of the inhomogeneity problem

The GDD algorithm for microtubule-based nucleation appeared almost insensitive to the cylindrical geometry, with very similar occurrences of longitudinal and transverse arrays. In contrast, on periodic (square) geometries, GDD was the only algorithm that showed a preference for certain orientations (Figure S3). These preferred orientations corresponded to the orientations of short closed paths that wrap around the geometry. This effect was most pronounced close to the transition to order (Figure S3D-F). Studying snapshots of individual simulations with such specific orientations showed that in these cases, there often was a single superbundle with the specific orientation, which wrapped back upon itself and with time absorbed most microtubule mass. With GDD microtubule-based nucleation, the parallel nucleations on the closed bundle increase its density, and, thereby, further increase the proportion of nucleations occuring from the closed bundle. With isotropic nucleation as well as with the new LDD microtubule-based nucleation, the additional density on the same bundle has no effect on the fraction of nucleations occurring from that bundle. So, only with GDD microtubule-based nucleation there is a positive feedback loop favouring closed superbundles and the corresponding array orientations. This GDD behaviour must, therefore, be considered an artefact of an inadequate algorithm for microtubule-based nucleation.

On cylinders, the available closed paths are transverse and longitudinal. These coincide with the most adopted orientations with all nucleation modes (Figures 4, S8) Time traces of individual simulations on cylinders (Figure S8), nonetheless, show a difference in behaviour between GDD and the other two nucleation modes. With GDD microtubule-based nucleation, the array often adopted the closed path orientation closest to the initial array orientation, with almost no traces crossing the midline ($\pm$ 45° away from transverse). For snapshots of an example simulation, see Figure S9A. With the other two nucleation modes, however, multiple arrays (from n=50) were observed that reoriented from longitudinal to transverse (Figure S8A,B,E,F; for snapshots, see Figure S9B). Again, the deviating array behaviour with GDD could be explained from the strong positive feedback on closed bundles with GDD microtubule-based nucleation only: once a closed bundle is formed, the probability that a competing orientation established keeps decreasing with time, because the array outside the closed bundle is slowly drained.

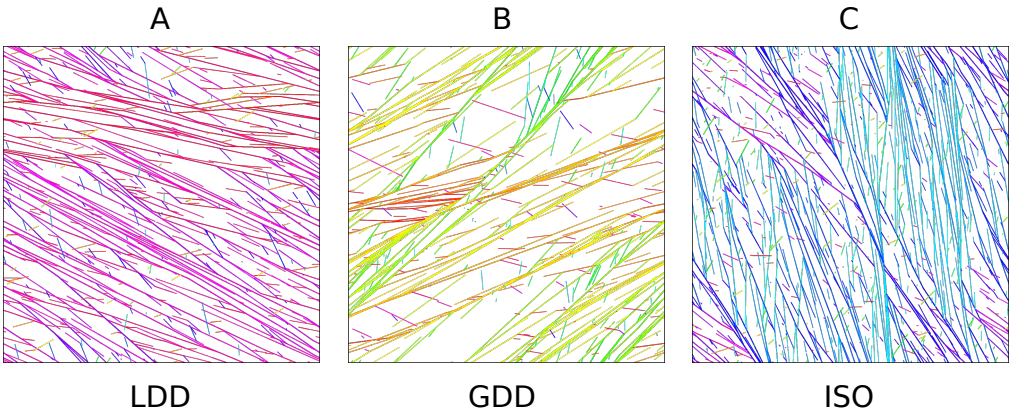


Figure 6: **Local domain formation is much less pronounced in arrays obtained through LDD than through GDD and ISO nucleation modes.** Snapshot at $T = 3 \times 10^4$ s (8 h, 20 min) of the microtubule array in a periodic square simulation domain of $80 \times 80$ $\mu$m$^2$ for (A) LDD: $S_2 = 0.90$, $G = -0.19$, (B) GDD: $S_2 = 0.90$, $G = -0.19$, and (C) ISO: $S_2 = 0.84$, $G = -0.14$. Different colours corresponds to different orientations for a microtubule or a bundle: warm colours correspond to transverse and cool colours to longitudinal orientations.

## Discussion

In this work, we have developed a novel, computational time efficient nucleation algorithm for realistic microtubule bound nucleation that does not suffer from the inhomogeneity problem that haunted the field for over a decade [12, 13, 16, 32]. We showed that different nucleation algorithms can have great impact on the overall behaviour of the cortical array. In particular, microtubule-based nucleation with local microtubule density-dependence extended the length and life time of microtubule bundles, thereby increasing the regime of spontaneous alignment and making the array more sensitive to subtle orientational cues from the cell's geometry. The ability to simulate this force realistically, opens up the possibility of quantitative comparison of different forces acting on array orientation.

A major open question in the field is how plant cells weigh different cues affecting the orientation of the cortical array. Such cues can be global, i.e., that always require information processing throughout the whole array, and local, i.e., that can be sensed (almost) everywhere in the cortex with similar intensity. The most prominent global cue derives directly from the cell geometry itself, as on many geometries, including cylinders, only a limited set of array orientations minimizes conflicts with itself [5, 19]. Cues like penalties for crossing (sharp) edges [5, 38] or cell faces with less favourable conditions can more selectively determine which orientations are realised [5, 19, 24]. In terms of information processing, these act as global cues.

In contrast, the co-alignment of microtubules with patterns of mechanical stress in the cell wall that seems to dominate in certain systems [20, 28, 36, 39–41], is typically assumed to happen via local cues, e.g., implemented as a slight bias in the microtubule growth direction towards the direction of (predicted) maximum wall stress [21], or increased growth propensity for co-aligned microtubules via the modulation of microtubule dynamics in simulation studies [24, 42]. The exact mechanism behind this observation remains elusive, but depends on katanin [36, 41]. This microtubule severing enzyme [43, 44] has a profound influence on alignment of the cortical array and is critically important

for array reorientation in response to various internal or external cues [35, 36, 41, 45, 46]. Another potential local cue is the tendency of some microtubules to slowly reorient such that they minimize their curvature either globally or over a small region, e.g., favouring longitudinal orientation on an infinite cylinder [37, 47, 48]. As these results all stem from theoretical work on non-interacting microtubules, the practical relevance of this tendency still is subject to debate. ALT: Recent simulations show that this effect indeed competes with global geometry based effects, including induced catastrophes at the edges of cylinders [49].

In our simulations on cylinders, reliably establishing a longitudinal orientation *de novo* seemed hard, i.e., it required stronger differences in the orientation dependent rescue rate than the maximum we tested. Although isotropic nucleation was more sensitive to this cue than the new LDD microtubule-based nucleation, we observed this with all nucleation modes that we tested. These simulations did not even include a form of microtubule alignment with cell wall stresses (e.g., [21]), which on a cylinder are twice as large for transverse compared to longitudinal [50]. Taken together, these factors seem at odds with the natural requirement of producing longitudinal arrays when necessary, e.g., when seedlings are first exposed to light or setting the longitudinal orientation of the S2 secondary cell wall layer in woody tissue [51]. Extensive work on dark-grown hypocotyls, however, shows that reorientation from transverse to longitudanal can be a very active process, in which, initially, the microtubules with the minority orientation are specifically amplified [22, 45, 52, 53]. A firm preference for the transverse orientation, therefore, would still be compatible with the occurrence of longitudinal arrays under specific conditions. Note, moreover, that other authors use more extreme orientation dependent variation in dynamic instability parameters before achieving reliable control over array orientation via such a mechanism. For example, Tian et al. [49] use a "modest" 80% increase in spontaneous catastrophe rate from most to least favoured orientation to overcome an opposing bias. Combined with a finite pool of total available tubulin and an active reorientation process, however, the required difference for selecting a preferred orientation from a transition state may be much smaller, e.g., a 10% difference in growth speed [22].

The question which cues are most important in orienting the microtubule array, therefore, also depends on the relative impact of local and global cues. The balance between local and global cues depends on the intrinsic (non-interacting) length of individual microtubules relative to the cell's dimensions, as this length scale affects how far and how easily the information of global cues propagates throughout the array [18] (also, compare Figure 4A and B). This balance can be further tuned towards local cues by reducing the microtubule persistence length [24, 25, 54] or towards global cues by increasing the persistence of microtubule bundles. We confirmed that microtubule-based nucleation, which has a substantial fraction of nucleations parallel or anti-parallel to the parent microtubule [23], can extend microtubule bundles and increase their life span [16]. As such, microtubule-based nucleation increases the relative impact of global orienting cues (compare LDD and isotropic nucleation in Figure 4). Such considerations emphasise the importance of microtubule simulations with a sufficient degree of realism in different aspects.

Here, our work plays a very import role. The algorithm we present allows for the efficient simulation of microtubule-based nucleation, whilst avoiding the problem of artificial inhomogeneity. Various experimental have shown that the responsiveness of array orientation to different cues critically depends on microtubule severing enzyme katanin [22, 36, 39, 41, 45, 52, 53]. With our new algorithm, the simulation platform CorticalSim now is equipped with both realistic katanin severing [35], semiflexible microtubules [25], and advanced microtubule-based nucleation.

Besides the competition between different cues affecting array orientation, our algorithm has

diverse other application areas. We name two additional examples. 1) The control of patterned secondary cell wall deposition, e.g., in xylem elements [12, 13, 25]. These regular patterns cannot be formed if the inhomogeneity problem appears, but timely separation of the array into future gaps and dense regions does require the positive feedback resulting from microtubule-based nucleation [13, 25]. 2) Consistent organ twisting and/or bending through the formation of helical arrays with predictable handedness [55,56], as observed, for example, in the *spiral* [57,58] and *lefty* mutants [59,60], in various mutants with point mutations in tubulin subunits that affect microtubule stability [61, 62], and following treatment with various drugs that affect microtubule stability [57,63]. What remains unclear is how changes in microtubule dynamics couple to chiral biases in the structure of microtubules, microtubule associated protein and/or the cell wall [64–66], and whether the array would adopt a fixed tilted orientation in isolated cells, or the observed array orientation would arise from a balance between competing rotating and counteracting forces, including tensile forces [67, 68], on the array. Again, we predict that the bundle elongating effect of microtubule-based nucleation will substantially impact such a balance. Another important question for organ twisting is how reliable array orientation at the level of single, isolated cells would need to be for a consistent, predictable outcome at the organ level, mediated through the mechanical coupling of cells and cell files [68]. Obviously, investigating this question would require integrating explicit microtubule simulations in a multi-level modelling approach.

Our computational advances enable the *in silico* investigation of the plant cortical array with unprecedented realism in a fast simulation environment. Compared to previous nucleation algorithms, this algorithm does not introduce artefacts related to the inhomogeneity problem as GDD-like algorithms [13, 16, 32], resulting in simulated cells that would have serious problems with cell wall integrity, but does offer the saturating, positive feedback on local microtubule density that is missing with isotropic nucleation, which supports patterning of the cortical array [12, 25] and increases the sensitivity to global cues. This advance supports a quantitative level of investigation that allows to distinguish between competing biophysical mechanisms. As illustrated by the examples above, there are many open questions beyond array orientation that can be addressed with help of our new algorithm.

# The model

We simulate the cortical array with an explicit stochastic platform, i.e., including all microtubules as sets of connected line segments that interact. The platform, CorticalSim, is a fast, event-based microtubule simulation platform written in C++ [11]. Table 1 summarizes model parameters and their default values.

## Microtubule dynamics

The dynamics of microtubules comprises two main components: intrinsic dynamics and microtubule-microtubule interaction. We employed the Dogterom and Leibler model [70] to describe the intrinsic dynamics of individual microtubules augmented with hybrid treadmilling [71], see Figure 1D. Microtubules can be either in the growing state, where they extend at the plus-end with a growth speed of $v^+$, or in the shrinking state, where they retract their plus-end with a shrinkage speed of $v^-$. The minus-end of microtubules retracts at a treadmilling speed of $v^{\mathrm{tm}}$ independently of the state of the plus-end. Transitions between the growing and shrinking states, and *vice versa*, occur

Table 1: Default model parameters.

| Parameter | Description | Value | Unit | Source |
|---|---|---|---|---|
| $v^+$ | Growth speed | 0.05 | $\mu$m s$^{-1}$ | [13] |
| $v^-$ | Shrinkage speed | 0.08 | $\mu$m s$^{-1}$ | [13] |
| $v^{\text{tm}}$ | Treadmilling speed | 0.01 | $\mu$m s$^{-1}$ | [13] |
| $r_c$ | Catastrophe rate | variable | s$^{-1}$ | |
| $r_r$ | Rescue rate | 0.001 | s$^{-1}$ | [13] |
| $\theta_c$ | Maximum collisional angle for bundling | 40° | - | [10] |
| $P_{\text{cat}}$ | Fraction of induced catastrophe after collision when $\theta > \theta_c$ | 0.5 | - | [35] |
| $r_n$ | Nucleation rate for ISO and GDD | 0.001 | $\mu$m$^{-2}$ s$^{-1}$ | [13] |
| $r_{\text{ins}}$ | Complex appearance rate for LDD | 0.0045 | $\mu$m$^{-2}$ s$^{-1}$ | [69] |
| $r_u$ | Per-complex unbound nucleation rate | 0.002 | s$^{-1}$ | [69] |
| $D$ | Diffusion coefficient of nucleation complexes | 0.013 | $\mu$m$^2$ s$^{-1}$ | [69] |
| $N$ | Number of meta-trajectories for LDD | 6 | - | |
| $R$ | Maximum meta-trajectory length for LDD | 1.5 | $\mu$m | |
| $P_{\text{rej},b}$ | Rejection probability for microtubule-based nucleation for LDD | 0.76 | - | [15] |
| $P_{\text{rej},u}$ | Rejection probability for unbound nucleation for LDD | 0.98 | - | [12] |
| $\rho_{1/2}$ | Tubulin density at which half of nucleations are isotropic for GDD | 0.1 | $\mu$m$^{-1}$ | [16] |
| $f_{\text{forward}}$ | Nucleation probability along the parent for GDD and LDD | 0.31 | - | [16] |
| $f_{\text{backward}}$ | Nucleation probability anti-parallel to the parent for GDD and LDD | 0.07 | - | [16] |
| $f_{\text{left}}$ | Nucleation probability to the left of the parent for GDD and LDD | 0.31 | - | [16] |
| $f_{\text{right}}$ | Nucleation probability to the right of the parent for GDD and LDD | 0.31 | - | [16] |
| $\epsilon$ | Ellipse eccentricity for GDD and LDD | 0.89 | - | [23] |
| $\theta_b$ | Mean branching angle for GDD and LDD | 35° | - | [23] |

with catastrophe and rescue rates denoted as $r_c$ and $r_r$, respectively.

When a growing microtubule plus end impinges on the lattice of another microtubule, the resulting type of interaction depends on the collision angle, comprised between 0° and 90°. For collision angles smaller than $\theta_c = 40°$, zippering occurs, causing the plus end to reorient alongside the encountered microtubule. When the collision angle is wider than 40°, the impinging plus-end has a probability $P_{\text{cat}}$ to undergo a collision-induced catastrophe, and a probability $1 - P_{\text{cat}}$ to create a cross-over with the other microtubule, see Figure 1E. Microtubule bundles emerge as a result of the zippering process. We assume that the collision between a growing microtubule tip and a bundle is equivalent to a collision with a single microtubule. Likewise, when a microtubule within a bundle collides with another microtubule, it remains unaffected by the presence of other microtubules within the same bundle. CorticalSim can simulate microtubule severing events induced by the severing enzyme katanin [35]. However, for simplicity, we do not consider katanin severing in this manuscript.

## Microtubule nucleation

We explore three distinct modes of microtubule nucleation: isotropic nucleation, global density-dependent nucleation, and a novel local density-dependent nucleation algorithm. The latter consists of a new computational approach, and we compare its performance against the former two methods, already well-studied in the literature [11, 16, 32, 33]. Regardless of the chosen nucleation mode, we assume that nucleation complex availability and behaviour are constant over time. The local density-dependent nucleation algorithm incorporates the following experimental observations: 1)

nucleation primarily occurs from the lattice of existing microtubules [15,23,30], 2) with a distribution of relative nucleation angles based on [23], and 3) observations of sparse, oryzalin treated, arrays show that nucleation complexes can appear in empty parts of the array, but have a higher nucleation efficiency after association with a microtubule [12, 15].

**Isotropic (ISO).** In the case of isotropic nucleation, new microtubules are nucleated at a rate $r_n$. The location and orientation are randomly selected with uniform probability.

**Global density-dependence (GDD).** In the global density-dependent nucleation (GDD) case, which was developed in [16], nucleation can be either microtubule-based or background unbound nucleation. Given the total density of tubulin $\rho$ used by microtubules, the rate at which microtubule-based nucleation occurs is

$$r_{n,\text{MT-based}} = r_n \frac{\rho}{\rho + \rho_{1/2}}, \tag{1}$$

where $\rho_{1/2}$ is an equilibrium constant determining the density at which half of the nucleations are microtubule-based [17]. Consequently, isotropic background nucleation occurs at a rate $r_{n,\text{unbound}} = (r_n - r_{n,\text{MT-based}})$. This approach aligns with observations, ensuring that initial nucleations in the microtubule-free membrane are unbound, while a small fraction of unbound nucleations occurs even at higher densities. In our simulations, the locations of microtubule-based nucleation events are uniformly distributed along the length of all available microtubules.

We modelled the angular distribution of microtubule-based nucleations as proposed by Deinum et al. [16]. Their nucleation mode includes three components: forward (towards the plus-end of the parent microtubule) with probability $f_{\text{forward}}$, backward (towards the minus-end of the parent microtubule) with probability $f_{\text{backward}}$, and the remaining probability sideways, split between left ($f_{\text{left}}$) and right ($f_{\text{right}}$). The sideways angles are modelled proportional to the relative partial surface area from a focal point of an ellipse with eccentricity $\epsilon$, with its main axis oriented with branching angle $\theta_b$ relative to the parent model. Parameters $\epsilon$ and $\theta_b$ are based on the data by Chan and Lloyd [23]. The full nucleation distribution function, denoted as $\nu(\theta)$, where $\theta$ is the angle between the direction of the parent and the daughter microtubules, combines these components:

$$\begin{aligned}\nu(\theta) = {} & f_{\text{forward}}\delta(\theta) + f_{\text{backward}}\delta(\theta - \pi) \\ & + \frac{(1-\epsilon^2)^{\frac{3}{2}}}{2\pi}\left[f_{\text{left}}\left(\frac{1}{1-\epsilon\cos(\theta-\theta_b)}\right)^2 + f_{\text{right}}\left(\frac{1}{1-\epsilon\cos(\theta+\theta_b)}\right)^2\right],\end{aligned} \tag{2}$$

where $\delta$ is the Dirac $\delta$-distribution.

**Local density-dependence (LDD).** New nucleation complexes appear at the membrane at rate $r_{\text{ins}}$ following the observation of nucleation complexes freely diffusing at the membrane [12]. These complexes are virtually placed at a random position $\mathbf{x}_0$ within the simulation domain. For convenience, and without loss of generality, we set $\mathbf{x}_0 = (0, 0)$ in the remainder of this section. To define a region for nucleation, we consider a circle with a radius $R$ centered at $\mathbf{x}_0$, which we call the nucleation area. Within this area, we draw $N$ radii, each referred to as a meta-trajectory. The first meta-trajectory is drawn at a random angle $\theta_1 \in [0, 2\pi)$ in the simulation domain, while subsequent meta-trajectories have angles $\theta_i = \theta_{i-1} + 2\pi/N$, see Figure 7A and B. A meta-trajectory labelled by $i$ may either intersect the lattice of a microtubule at a distance $r_i$ from the centre or reach the

boundary of the nucleation area, with $r_i$ being equal to the radius $R$ in the latter case. When a meta-trajectory intersects a microtubule lattice, it stops there (Figure 7B). We approximate the diffusion process by assuming that the nucleation complex can either reach these intersections by diffusion or diffuse away from the nucleation area. Here, we use $N = 6$ to reasonably represent the possible directions of diffusion of nucleation complexes.

Following the appearance of a nucleation complex at the membrane, three outcomes are possible: (i) the nucleation complex dissociates, (ii) an unbound nucleation occurs, (iii) or the complex reaches the lattice of a microtubule. After reaching a microtubule lattice (case iii), the complex may either produce a microtubule-based nucleation or dissociate before that. In experiments, the overall probability that a nucleation complex dissociated without nucleation depended on whether such a complex was freely diffusing or attached to a microtubule lattice. In the former case, the probability of dissociation is 98%, in the latter 76% [12, 15]. Ideally, the nucleation process should be modelled as a two-stage mechanism, with dissociation probabilities depending on time until reaching a microtubule lattice. Unfortunately, however, this cannot be parameterized with existing experimental data and performing the relevant measurements would be very challenging, because of the high density of most cortical arrays [12, 15]. We, therefore, adopt a pragmatic approach. We first determine the likelihood of a complex reaching a microtubule lattice, leading to a tentative microtubule-based or unbound nucleation event. Subsequently, part of the tentative nucleation events are rejected based on the above dissociation probabilities.

We assume a nucleation complex tentatively reaches a microtubule lattice if it does not produce an unbound nucleation before reaching the site via a 2D diffusion process. For this, we assume a constant unbound nucleation rate $r_u$, and take the time required to reach the site as the expected time for a mean squared displacement of distance $d_i$:

$$\tau_i = \frac{d_i^2}{4D}. \tag{3}$$

Consequently, the probability $p$ that a microtubule tentatively reaches the lattice intersected by the meta-trajectory $i$ before unbound nucleation is given by:

$$p(d_i) = 1 - \int_0^{\tau_i} \mathrm{d}t\, r_u e^{-r_u t} = e^{-r_u \frac{d_i^2}{4D}}. \tag{4}$$

Hence, $0.24p(d_i)$ is the probability of a microtubule-based nucleation on meta-trajectory $i$. Similarly, $0.02\,(1 - p(d_i))$ is the probability of unbound nucleation on meta-trajectory $i$. In our simulations, we used a maximum meta-trajectory length of $R = 1.5\mu$m because, given our choice of parameters values (Table 1), the probability $p(R)$ of a nucleation complex intersecting with a microtubule lattice prior to nucleation becomes negligible beyond this length. Based on this, the probability of microtubule-based nucleation after a nucleation complex appear at the membrane is

$$p_{\text{MT-based}} = \frac{0.24}{N} \sum_j p(r_j), \tag{5}$$

where the sum over $j$ only runs over meta-trajectories that intersect a microtubule, while the probability of unbound nucleation is $0.02(1 - p_{\text{MT-based}})$, see Figure 7C. Note that, for computational efficiency, one could equivalently use $r'_{\text{ins}} = r_{\text{ins}}/0.24$ and accept all tentative bound nucleations and accept tentative unbound nucleations with probability $0.083 = 0.02/0.24$.

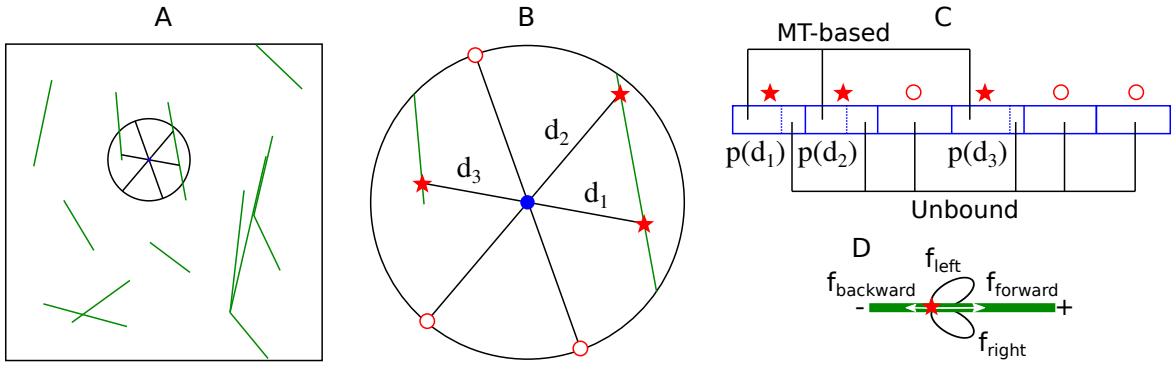


Figure 7: **Schematic overview of the LDD nucleation algorithm**. (A) The position in the simulation domain where a nucleation complex appears is selected randomly, with uniform distribution. (B) Such a position, represented by the blue circle, is the centre of the nucleation area (the area included in the black circumference). $N$ meta-trajectories are drawn equidistant from one another and with random orientation. Meta-trajectories are drawn up until the closer between the boundary of the nucleation area or the lattice of an intersecting microtubule. (C) Whether the resulting nucleation is microtubule-based or unbound and, in the former case, the parent microtubule and the nucleation location, is decided stochastically with probability $0.24p(r_i)$ weighted over the length of meta-trajectories, according to Equation (4). (D) In a microtubule-based nucleation, the angles follow [16]: a newly-nucleated microtubule initially grows along the parent microtubule with probability $f_{\text{forward}}$, in the opposite direction with probability $f_{\text{backward}}$, or branches to either side with probability $f_{\text{left/right}}$. The branching angle is determined according to a distribution that closely matches the data in [23].

## Degree of alignment and orientation of the array

To assess the alignment of microtubules in a planar system, we use a nematic order parameter $S_2$ that accounts for the contribution of individual microtubule segments proportionally weighted on their length [16]. For planar geometries, $S_2$ is defined by

$$S_2 = \sqrt{\langle\langle \cos 2\theta \rangle\rangle^2 + \langle\langle \sin 2\theta \rangle\rangle^2}, \tag{6}$$

where the double brackets denote a length-weighted average over all microtubule segments. $S_2$ has a value of 0 for an isotropic system and a value of 1 for a system where microtubules are perfectly aligned. For non-planar geometries, we use the order parameter $R_2 \in [0, 1]$ which extends the definition of nematic order parameter to surfaces in the 3D space as defined in [11]. At the $S_2$ order parameter in 3D would produce non-zero values for isotropic arrays on cylinders, because of the confinement the microtubules to the surface, the definition of $R_2$ includes a correction for the expected value for a fully isotropic array. Consequently, the maximum $R_2$ value depends on array orientation: it is 1 for transverse arrays and (1+D/L)/2 for cylindrical arrays with length L > diameter D. The minimal value is always 0. Only in Figure S8, $R_2$ values are renormalized by this maximum.

We couple the alignment order parameter $S_2$ with the overall array orientation $\Theta_2$:

$$\Theta_2 = \arctan\left(\frac{\langle\langle \sin 2\theta \rangle\rangle}{\langle\langle \cos 2\theta \rangle\rangle + S_2}\right). \tag{7}$$

On non-planar geometries (only capped cylinders in this manuscript), we use the definition of orientation vector $\Theta_2$ coupled to $R_2$ [11]. This the angle between the cylinder axis and the direction most *avoided* by the array, i.e., the predicted preferred direction of cell expansion. Note that this is the opposite of $S_2$-based $\Theta_2$. We, therefore, indicate the longitudinal and transverse orientation alongside the relevant Figures to avoid confusion.

## Navigating parameter space with control parameter $G$

The driver of spontaneous alignment in the cortical array is the occurrence of sufficient interactions within the average microtubule length. This is quantified by a single control parameter $G$ [8, 9], which is the ratio of two length scales: an interaction length scale (left factor) and the average length of non-interacting microtubules (right factor). We use a version of $G$ adjusted for minus end treadmilling [16]:

$$G = \left(\frac{2(v^+ - v^{\mathrm{tm}})^2(v^- + v^{\mathrm{tm}})}{r_n v^+(v^+ + v^-)}\right)^{1/3}\left(\frac{r_r}{v^- + v^{\mathrm{tm}}} - \frac{r_c}{v^+ - v^{\mathrm{tm}}}\right). \tag{8}$$

Note that we restrict ourselves to $G < 0$, i.e., when microtubules are in the so-called bounded-growth regime, where they have a finite life span and finite intrinsic length. In this case, spontaneous alignment occurs if $G > G^*$, some threshold that depends on the details of microtubule-microtubule interactions. In graphs where we vary $G$, we use the notation $G_c$ to indicate that $G$ is varied via $r_c$.

For ISO and GDD nucleation modes, the nucleation rate $r_n$ is an explicit simulation parameter. For LDD nucleation, however, $r_n$ results from the interplay between the rate at which nucleation complexes appear at the membrane $r_{\mathrm{ins}}$ and rejection of nucleations, which in turn depends on the density and distribution of the microtubules. Therefore, we calculate the effective nucleation rate to be used for $G$ in Equation (8) as

$$r_n = \frac{n_c(T)}{TA}, \tag{9}$$

where $n_c(T)$ is the number of nucleation events occurred after time $T$, and $A$ is the area of the simulation domain. In principle, $n_c$ might be non-linear in $T$, making our proposed computation of $r_n$ overly-simplistic. However, our test showed that $n_c(T)$ is approximately linear in $T$, for $T < 3 \times 10^4$ s (8 h, 20 min), see Figure S2.

## Global and local bias on cylindrical geometry

We incorporated two distinct directional biases independently: a global bias, represented by an 8% increase in the catastrophe rate $r_c$ at the cylinder caps, and a local bias, with a maximum $b_{\max}$ (default: 8%) orientation dependent increase of the rescue rate $r_r$ for individual microtubules. The increase was implemented as:

$$r_{r,\mathrm{extra}} = \frac{b_{\max}}{2}\left[1 + \cos\left(2(\theta - \theta_r)\right)\right], \tag{10}$$

where $\theta$ denotes the orientation of the microtubule plus end, $\theta_r$ represents the angle at which the rescue rate is maximum, and $b_{\max}$ (default = 0.08) is the maximal increase factor when $\theta = \theta_r$.

## References


[1] Ehrhardt DW, Shaw SL. Microtubule dynamics and organization in the plant cortical array. Annual Review of Plant Biology. 2006;57:859–75.

[2] Sablowski R. Coordination of plant cell growth and division: collective control or mutual agreement? Current Opinion in Plant Biology. 2016;34:54–60.

[3] Wasteneys GO. Microtubule organization in the green kingdom: chaos or self-order? Journal of Cell Science. 2002;115:1345.

[4] Chan J, Coen E. Interaction between autonomous and microtubule guidance systems controls cellulose synthase trajectories. Current Biology. 2020;30(5):941–947.

[5] Chakrabortty B, Willemsen V, de Zeeuw T, Liao CY, Weijers D, Mulder B, et al. A plausible microtubule-based mechanism for cell division orientation in plant embryogenesis. Current Biology. 2018;28(19):3031–3043.

[6] Gutierrez R, Lindeboom JJ, Paredez AR, Emons AM, Ehrhardt DW. Arabidopsis cortical microtubules position cellulose synthase delivery to the plasma membrane and interact with cellulose synthase trafficking compartments. Nature Cell Biology. 2009;11(7):797–806.

[7] Paredez AR, Somerville CR, Ehrhardt DW. Visualization of Cellulose Synthase Demonstrates Functional Association with Microtubules. Science. 2006;312(5779):1491–1495.

[8] Tindemans SH, Hawkins RJ, Mulder BM. Survival of the aligned: ordering of the plant cortical microtubule array. Phys Rev Lett. 2010;104(5):058103.

[9] Deinum EE, Mulder BM. Modelling the role of microtubules in plant cell morphology. Curr Opin Plant Biol. 2013;16(6):688–692.

[10] Dixit R, Cyr R. Encounters between Dynamic Cortical Microtubules Promote Ordering of the Cortical Array through Angle-Dependent Modifications of Microtubule Behavior. The Plant Cell. 2004;16(12):3274–3284.

[11] Tindemans SH, Deinum EE, Lindeboom JJ, Mulder B. Efficient event-driven simulations shed new light on microtubule organisation in the plant cortical array. Frontiers in Physics. 2014;2(19):9.

[12] Jacobs B, Schneider R, Molenaar J, Filion L, Deinum EE. Microtubule nucleation complex behavior is critical for cortical array homogeneity *and* xylem wall patterning. Proceedings of the National Academy of Sciences. 2022;119(50):e2203900119.

[13] Schneider R, Klooster Kv, Picard KL, van der Gucht J, Demura T, Janson M, et al. Long-term single-cell imaging and simulations of microtubules reveal principles behind wall patterning during proto-xylem development. Nature communications. 2021;12(1):1–12.

[14] Sambade A, Pratap A, Buschmann H, Morris RJ, Lloyd C. The influence of light on microtubule dynamics and alignment in the Arabidopsis hypocotyl. Plant Cell. 2012;24(1):192–201.

[15] Nakamura M, Ehrhardt DW, Hashimoti T. Microtubule and katanin-dependent dynamics of microtubule nucleation complexes in the acentrosomal Arabidopsis cortical array. Nature Cell Biology. 2010;12(11):1064–70.

[16] Deinum EE, Tindemans SH, Mulder BM. Taking directions: the role of microtubule-bound nucleation in the self-organization of the plant cortical array. Phys Biol. 2011;8(5):056002.

[17] Foteinopoulos P, Mulder BM. The effect of anisotropic microtubule-bound nucleations on ordering in the plant cortical array. Bulletin of mathematical biology. 2014;76(11):2907–2922.

[18] Chakrabortty B, Blilou I, Scheres B, Mulder BM. A computational framework for cortical microtubule dynamics in realistically shaped plant cells. PLoS computational biology. 2018;14(2):e1005959.

[19] Deinum EE, Mulder BM. Modelling the Plant Microtubule Cytoskeleton. In: Morris RJ, editor. Mathematical Modelling in Plant Biology. Springer; 2018. p. 53–67.

[20] Hamant O, Heisler MG, Jonsson H, Krupinski P, Uyttewaal M, Bokov P, et al. Developmental patterning by mechanical signals in Arabidopsis. Science. 2008;322(5908):1650–5.

[21] Mirabet V, Krupinski P, Hamant O, Meyerowitz EM, Jönsson H, Boudaoud A. The self-organization of plant microtubules inside the cell volume yields their cortical localization, stable alignment, and sensitivity to external cues. PLoS computational biology. 2018;14(2):e1006011.

[22] Saltini M, Mulder BM. A plausible mechanism for longitudinal lock-in of the plant cortical microtubule array after light-induced reorientation. Quantitative Plant Biology. 2021;2:e9.

[23] Chan J, Sambade A, Calder G, Lloyd C. Arabidopsis Cortical Microtubules Are Initiated along, as Well as Branching from, Existing Microtubules. Plant Cell. 2009;12(8):2298–306.

[24] Saltini M, Deinum EE. Microtubule simulations in plant biology: a field coming to maturity. Curr Opin Plant Biol. 2024;doi:10.1016/j.pbi.2024.102596.

[25] Jacobs B, Saltini M, Molenaar J, Filion LC, Deinum EE. Protoxylem microtubule patterning requires ROP pattern co-alignment, realistic microtubule-based nucleation, and sufficient microtubule flexibility. bioRxiv. 2024;doi:https://doi.org/10.1101/2024.04.04.588070.

[26] Hawkins T, Mirigian M, Yasar MS, Ross JL. Mechanics of microtubules. Journal of biomechanics. 2010;43(1):23–30.

[27] Durand-Smet P, Spelman TA, Meyerowitz EM, Jönsson H. Cytoskeletal organization in isolated plant cells under geometry control. Proceedings of the National Academy of Sciences. 2020;117(29):17399–17408.

[28] Colin L, Chevallier A, Tsugawa S, Gacon F, Godin C, Viasnoff V, et al. Cortical tension overrides geometrical cues to orient microtubules in confined protoplasts. Proceedings of the National Academy of Sciences. 2020;.

[29] Gomez JM, Chumakova L, Bulgakova NA, Brown NH. Microtubule organization is determined by the shape of epithelial cells. Nature Communication. 2016;7:13172.

[30] Murata T, Sonobe S, Baskin TI, Hyodo S, Hasezawa S, Nagata T, et al. Microtubule-dependent microtubule nucleation based on recruitment of gamma-tubulin in higher plants. Nature Cell Biology. 2005;7(10):961–8.

[31] Yagi N, Fujita S, Nakamura M. Plant microtubule nucleating apparatus and its potential signaling pathway. Current Opinion in Plant Biology. 2024;82:102624. doi:https://doi.org/10.1016/j.pbi.2024.102624.

[32] Allard JF, Wasteneys GO, Cytrynbaum EN. Mechanisms of self-organization of cortical microtubules in plants revealed by computational simulations. Molecular Biology of the Cell. 2010;21(2):278–86.

[33] Eren EC, Dixit R, Gautam N. A 3D Computer Simulation Model Reveals the Mechanisms for Self-Organization of Plant Cortical Microtubules into Oblique Arrays. Mol Biol Cell. 2010;21(15):2674–84.

[34] Motta MR, Nedelec F, Woelken E, Saville H, Jacquerie C, Pastuglia M, et al. The cell cycle controls spindle architecture in Arabidopsis by modulating the augmin pathway. bioRxiv. 2023; p. 2023–11.

[35] Deinum EE, Tindemans SH, Lindeboom JJ, Mulder BM. How selective severing by katanin promotes order in the plant cortical microtubule array. Proceedings of the National Academy of Sciences. 2017;114(27):6942–6947.

[36] Eng RC, Schneider R, Matz TW, Carter R, Ehrhardt DW, Jönsson H, et al. KATANIN and CLASP function at different spatial scales to mediate microtubule response to mechanical stress in Arabidopsis cotyledons. Current Biology. 2021;.

[37] Tian TY, Macdonald CB, Cytrynbaum EN. A stochastic model of cortical microtubule anchoring and mechanics provides regulatory control of microtubule shape. Bulletin of Mathematical Biology. 2023;85(11):1–23.

[38] Ambrose C, Allard JF, Cytrynbaum EN, Wasteneys GO. A CLASP-modulated cell edge barrier mechanism drives cell-wide cortical microtubule organization in *Arabidopsis*. Nature Communication. 2011;2:430.

[39] Uyttewaal M, Burian A, Alim K, Landrein B, Borowska-Wykret D, Dedieu A, et al. Mechanical stress acts via katanin to amplify differences in growth rate between adjacent cells in *Arabidopsis*. Cell. 2012;149:439.

[40] Louveaux M, Julien JD, Mirabet V, Boudaoud A, Hamant O. Cell division plane orientation based on tensile stress in *Arabidopsis thaliana*. Proceedings of the National Academy of Science. 2016;113:E4294.

[41] Sampathkumar A, Krupinski P, Wightman R, Milani P, Berquand A, Boudaoud A, et al. Subcellular and supracellular mechanical stress prescribes cytoskeleton behavior in Arabidopsis cotyledon pavement cells. Elife. 2014;3:e01967.

[42] Smithers ET. Using mathematical modelling to understand how plant cell growth is controlled. University of Birmingham; 2022.

[43] Burk DH, Liu B, Zhong R, Morrison WH, Ye ZH. A Katanin-like Protein Regulates Normal Cell Wall Biosynthesis and Cell Elongation. THE PLANT CELL. 2001;13(4):807.

[44] Bichet A, Desnos T, Turner S, Grandjean O, Höfte H. BOTERO1 is required for normal orientation of cortical microtubules and anisotropic cell expansion in Arabidopsis. The Plant Journal. 2001;25(2):137–148.

[45] Lindeboom JJ, Nakamura M, Hibbel A, Shundyak K, Gutierrez R, Ketelaar T, et al. A mechanism for reorientation of cortical microtubule arrays driven by microtubule severing. Science. 2013;342(6163):1245533.

[46] Saltini M, Mulder BM. Critical threshold for microtubule amplification through templated severing. Physical Review E. 2020;101:052405.

[47] Cosentino Lagomarsino M, Tanase C, Vos JW, Emons AMC, Mulder BM, Dogterom M. Microtubule Organization in Three-Dimensional Confined Geometries: Evaluating the Role of Elasticity Through a Combined In Vitro and Modeling Approach. Biophysical Journal. 2007;92(3):1046.

[48] Bachmann S, Froese R, Cytrynbaum EN. A buckling instability and its influence on microtubule orientation in plant cells. SIAM Journal on Applied Mathematics. 2019;79(5):2132–2149.

[49] Tian TY, Wasteneys GO, Macdonald CB, Cytrynbaum EN. Cell geometry, microtubule anchoring and anisotropic dynamic instability: challenges and solutions to transverse cortical array organization. bioRxiv. 2024; p. 2024–09. doi:10.1101/2024.09.07.611822.

[50] Geitmann A, Ortega JK. Mechanics and modeling of plant cell growth. Trends Plant Sci. 2009;14(9):467–78. doi:10.1016/j.tplants.2009.07.006.

[51] Deinum EE. The systems and interactions underpinning complex cell wall patterning. Biochemical Society Transactions. 2024; p. BST20230642. doi:10.1042/BST20230642.

[52] Lindeboom JJ, Nakamura M, Saltini M, Hibbel A, Walia A, Ketelaar T, et al. CLASP stabilization of plus ends created by severing promotes microtubule creation and reorientation. Journal of Cell Biology. 2019;218(1):190–205.

[53] Nakamura M, Lindeboom JJ, Saltini M, Mulder BM, Ehrhardt DW. SPR2 protects minus ends to promote severing and reorientation of plant cortical microtubule arrays. Journal of Cell Biology. 2018;217(3):915–927.

[54] Sasaki T, Saito K, Inoue D, Serk H, Sugiyama Y, Pesquet E, et al. Confined-microtubule assembly shapes three-dimensional cell wall structures in xylem vessels. Nature Communications. 2023;14(1):6987.

[55] Wada H. Hierarchical helical order in the twisted growth of plant organs. Phys Rev Lett. 2012;109(12):128104.

[56] Buschmann H, Borchers A. Handedness in plant cell expansion: a mutant perspective on helical growth. New Phytologist. 2020;225:53–56.

[57] Furutani I, Watanabe Y, Prieto R, Masukawa M, Suzuki K, Naoi K, et al. The *SPIRAL* genes are required for directional control of cell elongation in *Arabidopsis thaliana*. Development. 2000;127:4443–53.

[58] Nakamura M, Hashimoto T. A mutation in the Arabidopsis gamma-tubulin-containing complex causes helical growth and abnormal microtubule branching. Journal of Cell Science. 2009;122:2208–17.

[59] Thitamadee S, Tuchihara K, Hashimoto T. Microtubule basis for left-handed helical growth in Arabidopsis. Nature. 2002;417(6885):193–196.

[60] Sunohara H, Kawai T, Shimizu-Sato S, Sato Y, Sato K, Kitano H. A dominant mutation of TWISTED DWARF 1 encoding an $\alpha$-tubulin protein causes severe dwarfism and right helical growth in rice. Genes & genetic systems. 2009;84(3):209–218.

[61] Ishida T, Kaneko Y, Iwano M, Hashimoto T. Helical microtubule arrays in a collection of twisting tubulin mutants of Arabidopsis thaliana. Proceedings of the National Academy of Science. 2007;104(20):8544–9.

[62] Buschmann H, Hauptmann M, Niessing D, Lloyd CW, Schäffner AR. Helical growth of the Arabidopsis mutant tortifolia2 does not depend on cell division patterns but involves handed twisting of isolated cells. The Plant Cell. 2009;21(7):2090–2106.

[63] Nakamura M, Naoi K, Shoji T, Hashimoto T. Low concentrations of propyzamide and oryzalin alter microtubule dynamics in Arabidopsis epidermal cells. Plant and cell physiology. 2004;45(9):1330–1334.

[64] Landrein B, Lathe R, Bringmann M, Vouillot C, Ivakov A, Boudaoud A, et al. Impaired cellulose synthase guidance leads to stem torsion and twists phyllotactic patterns in Arabidopsis. Curr Biol. 2013;23(10):895–900. doi:10.1016/j.cub.2013.04.013.

[65] Liu Z, Schneider R, Kesten C, Zhang Y, Somssich M, Zhang Y, et al. Cellulose-Microtubule Uncoupling Proteins Prevent Lateral Displacement of Microtubules during Cellulose Synthesis in Arabidopsis. Developmental Cell. 2016;38(3):305 – 315. doi:http://dx.doi.org/10.1016/j.devcel.2016.06.032.

[66] Saffer AM, Carpita NC, Irish VF. Rhamnose-containing cell wall polymers suppress helical plant growth independently of microtubule orientation. Current Biology. 2017;27(15):2248–2259.

[67] Chan J, Calder G, Fox S, Lloyd C. Cortical microtubule arrays undergo rotary movements in Arabidopsis hypocotyl epidermal cells. Nature Cell Biology. 2007;9(2):171–5.

[68] Verger S, Liu M, Hamant O. Mechanical conflicts in twisting growth revealed by cell-cell adhesion defects. Frontiers in plant science. 2019;10:173.

[69] Jacobs B. Exploring mechanisms of xylem cell wall patterning with dynamic models. Wageningen University and Research; 2022.

[70] Dogterom M, Leibler S. Physical aspects of the growth and regulation of microtubule structures. Physical Review Letters. 1993;70:1347.

[71] Shaw SL, Kamyar R, Ehrhardt DW. Sustained Microtubule Treadmilling in Arabidopsis Cortical Arrays. Science. 2003;300(5626):1715–1718.

# Supplementary Figures

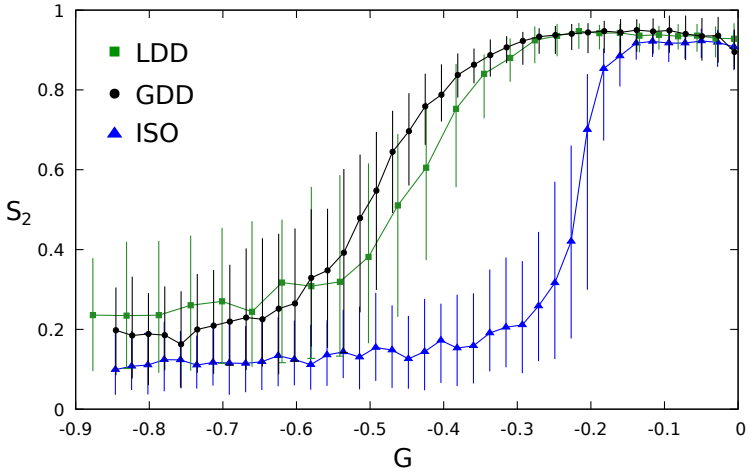


Figure S1: Median over 100 independent simulation runs of the order parameter $S_2$ as function of the control parameter $G$ at $T = 3 \times 10^4$ s (8 h, 20 min), for LDD, GDD, and ISO nucleation modes in a squared geometry with sizes $L = 40\mu$m and $H = 40\mu$m, as depicted in Figure 3. Error bars represent the 10th and 90th percentile.

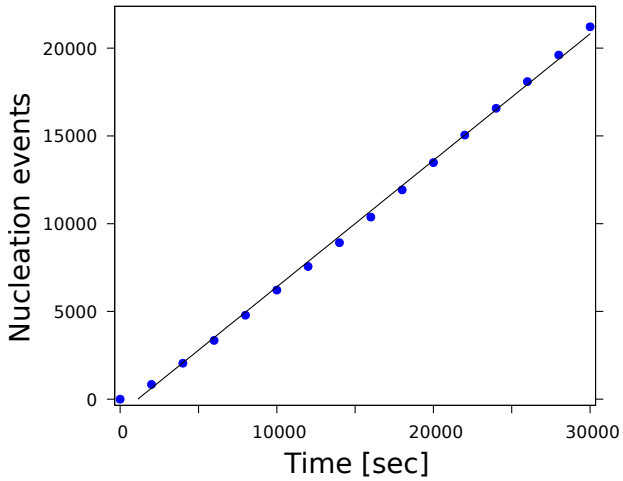


Figure S2: **The nucleation rate remains roughly constant throughout the simulation.** Cumulative number of nucleation events as a function of time for one simulation run with LDD nucleation mode and in a square simulation domain with periodic boundary conditions and size $L = 40\mu$m. The black line corresponds to the fitting function $f(t) = a + bt$, with $a = -809 \pm 153$ and $b = 0.72 \pm 0.01$. In this simulation, $r_c = 0.0025$ s$^{-1}$.

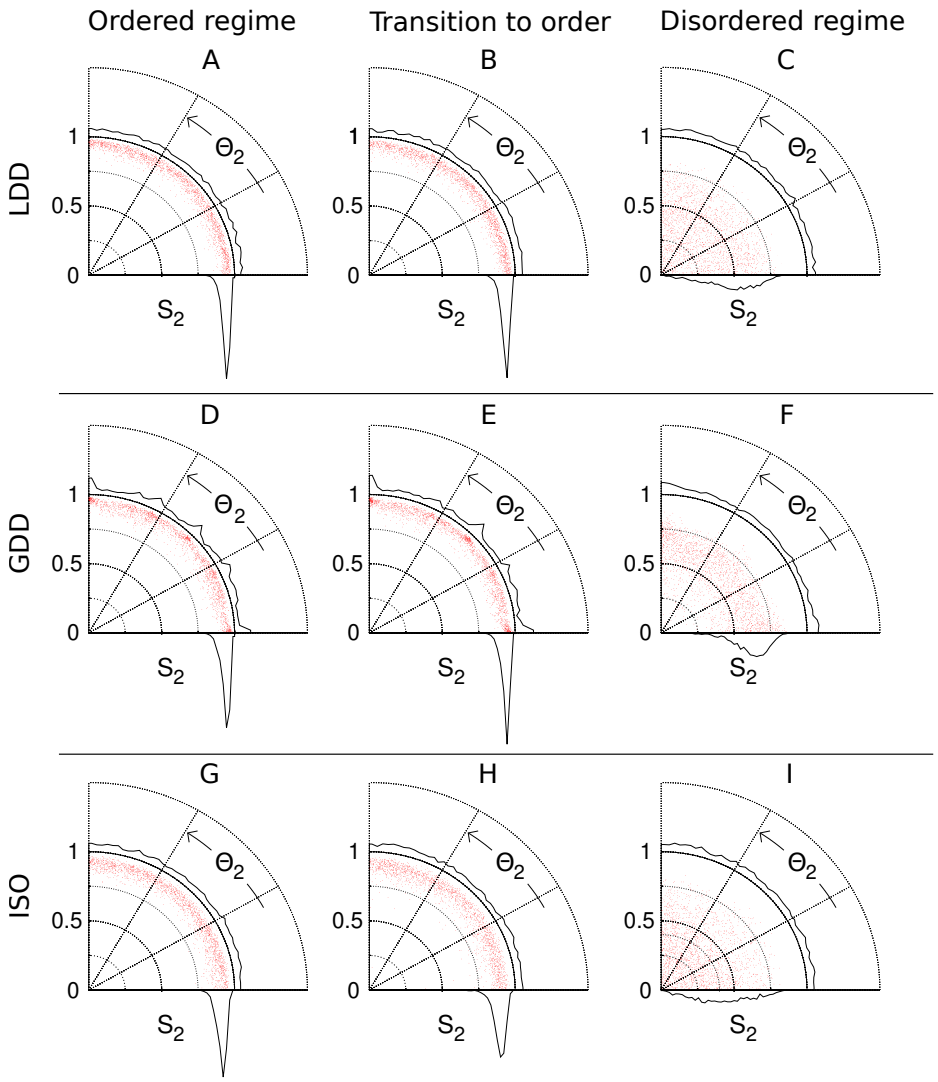


Figure S3: **LDD nucleation is bias-free for orientation on a square periodic geometry**, suggesting that the previously reported preference for the shortest few closed paths around a geometry with GDD was a consequence of the inhomogeneity problem. Distribution of $S_2$ and $\Theta_2$ for three different regimes . Each panel contains the result in terms of alignment $S_2$ and orientation $\Theta_2$ of 2000 independent runs at $T = 3 \times 10^4$ s (8 h, 20 min). A point located along the horizontal axis represents a perfectly transverse array orientation, while a point on the vertical axis represents a perfectly longitudinal orientation. The distance of the point from the origin indicates the strength of the alignment, with greater distances indicating a higher degree of alignment. The data points are collected to generate histograms for the distribution of $S_2$ (horizontal axis) and $\Theta_2$ (vertical axis). $G$ values: (A) $G = -0.22$, (B) $G = -0.25$, (C) $G = -0.42$, (D) $G = -0.23$, (E) $G = -0.25$, (F) $G = -0.54$, (G) $G = -0.16$, (H) $G = -0.18$, (I) $G = -0.25$. Panels (A), (D), and (G) correspond to the empty markers of Figure 3A.

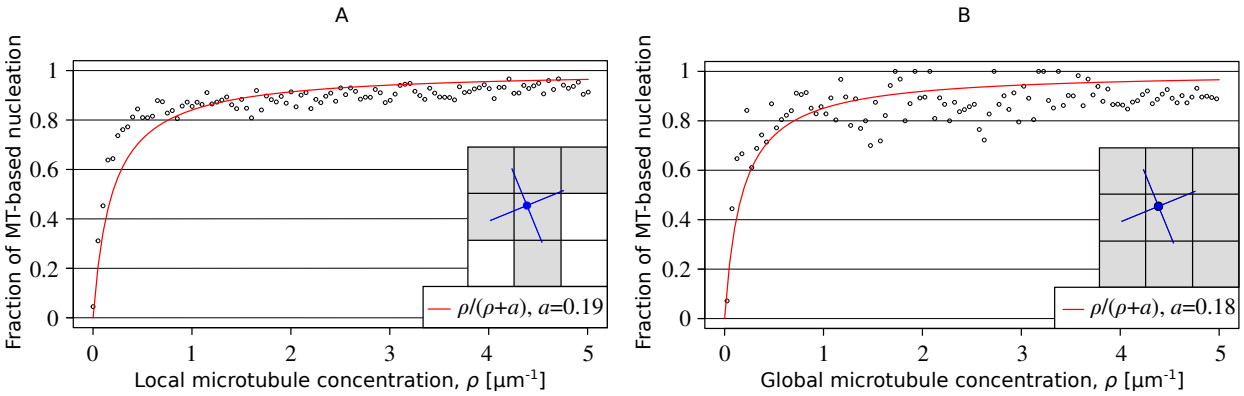


Figure S4: **LDD microtubule-based nucleation naturally results in a local microtubule density-dependent fraction of microtubule-based nucleation**. Fraction of microtubule-based nucleation as a function of (A) local and (B) global microtubule density ($\rho$) during a single simulation run. In this simulation, $r_c = 0.0025$ s$^{-1}$. The global microtubule density (B) was computed as expected as $\rho = \sum_i l_i/A$, where $l_i$ represents the length of the $i$-th microtubule, the summation runs over all microtubules, and $A$ denotes the area of the simulation domain. The local microtubule density (A) was determined via $\rho = \sum_{i,j} l_{i_j} / \sum_j A_j$. In this expression, $l_{i_j}$ represents the length of the segment of the $i$-th microtubule within region $j$ with area $A_j$, and $j$ runs over all regions touched by the metatrajectories drawn from the appearance point of a nucleation complex, as shown by the schematic in panel A. The curves fit through the data are of the same shape as the formula used for determining the fraction of microtubule-based nucleation with the old GDD microtubule-based nucleation algorithm.

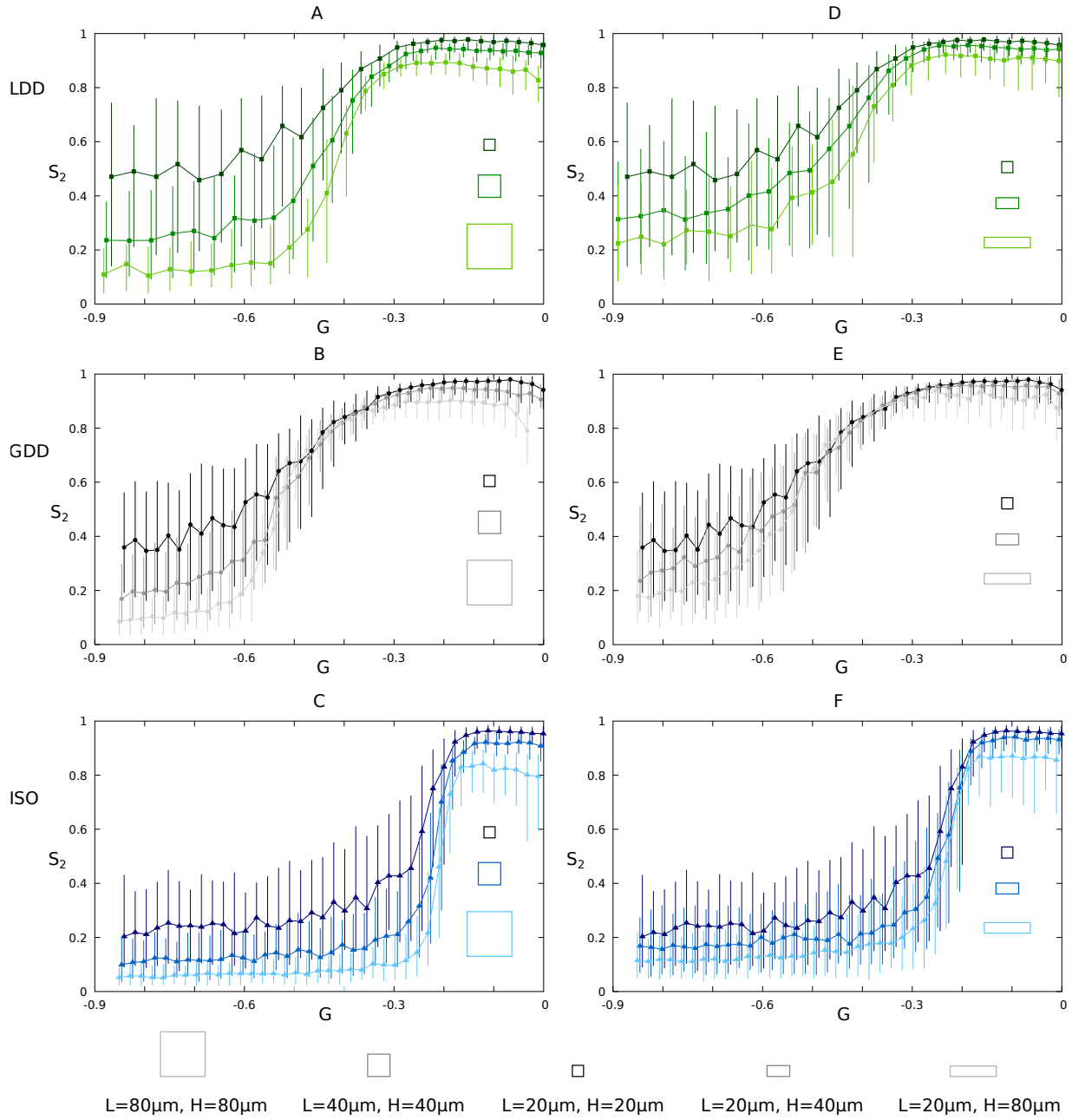


Figure S5: **Dependence of global alignment on geometry size and aspect ratio for all nucleation modes.** Median over 100 simulation runs of the degree of alignment $S_2$ as a function of the control parameter $G$ for LDD, GDD, and ISO nucleation modes for (A-C) increasing size and (D-F) increasing height-to-length aspect ratio of the planar periodic simulation domain, at $T = 3 \times 10^4$ s (8 h, 20 min). (B,C,E,F) In the ISO and GDD cases, results for the $L = 20\mu$m, $H = 20\mu$m grid are shifted to the right on the $G$ axis by 0.005, whereas results for the $L = 80\mu$m, $H = 80\mu$m and the $L = 20\mu$m, $H = 80\mu$m grids are shifted to the left by 0.005 for visibility of the error bars. Error bars represent the $10^{\text{th}}$ to $90^{\text{th}}$ percentile.

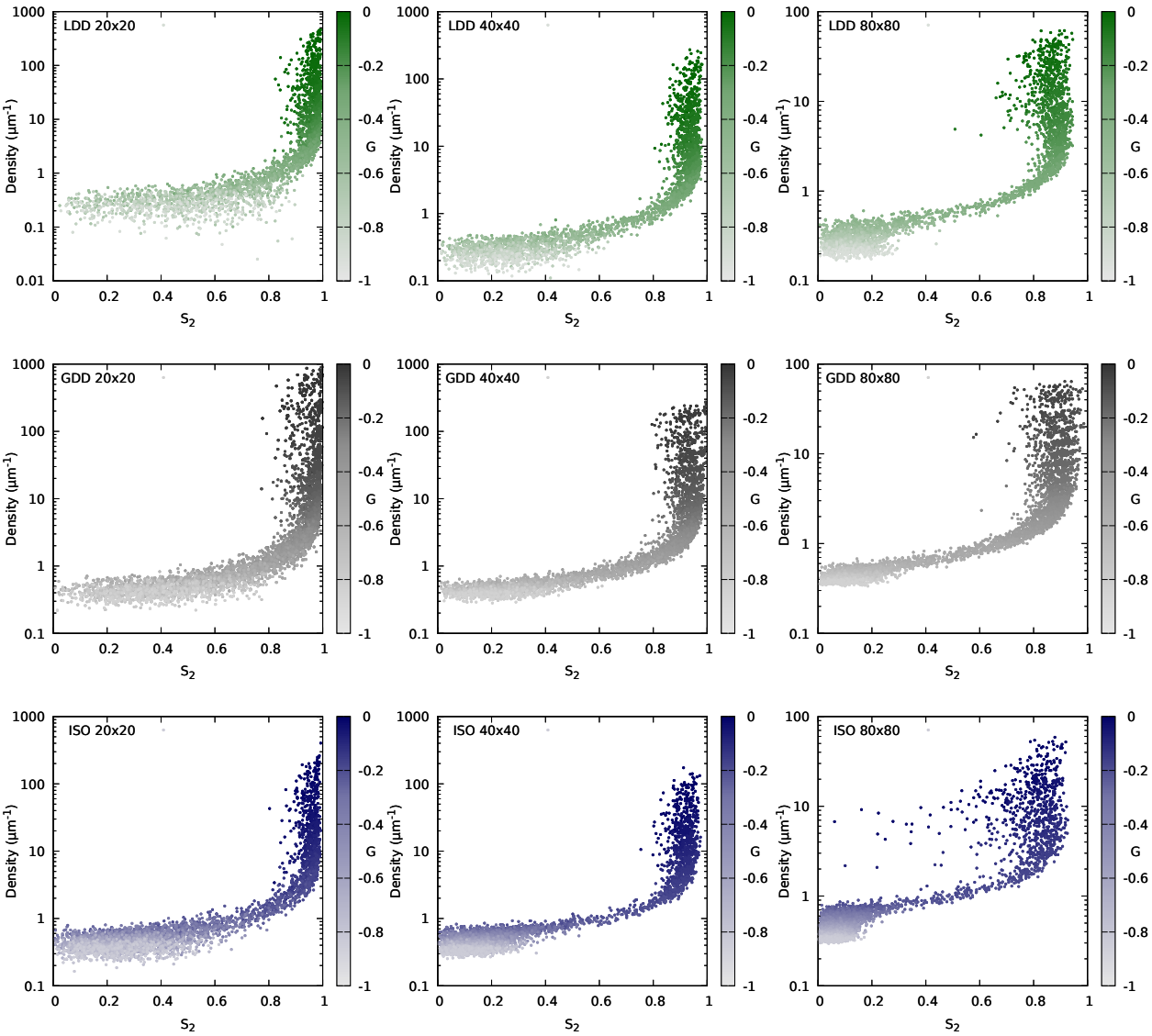


Figure S6: **Clear signs of local domain formation with isotropic nucleation on large (80x80 $\mu$m$^2$ periodic) simulation domains**. Scatter plots of density as a function of $S_2$, coloured by $G$ for the three nucleation modes (rows: LDD, GDD, ISO) and three domain sizes (columns: 20x20, 40x40 and 80x80 $\mu$m$^2$) as indicated in the graphs, at $T = 3 \times 10^4$ s (8 h, 20 min). Most points fall on a curve from low density and low $S_2$ to high density and high $S_2$ with increasing $G$. Points with relatively high $G$ and density, but distinctly lower $S_2$ that other points with similar $G$ and density are in the regime of spontaneous alignment, but the occurrence of multiple aligned domains with different orientations reduces the global $S_2$. The most and most severe cases occur with isotropic nucleation on the largest domains. These plots are based on the same data as Figure S5, with 100 simulations per (target) $G$ value. (Lower for the highest $G$ values for LDD and GDD, because not all simulations terminated in time).

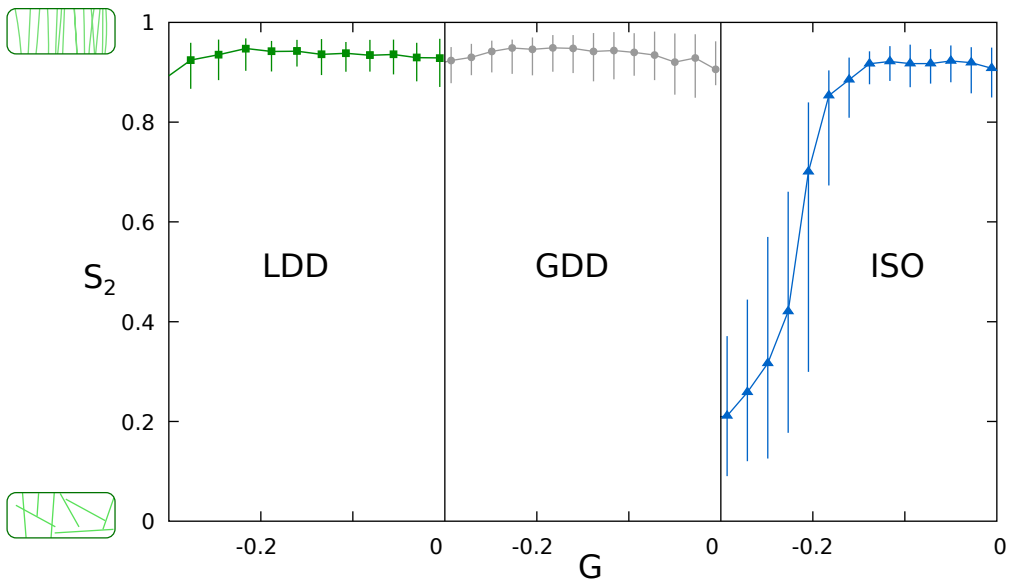


Figure S7: Comparison of the regime of alignment in a square domain ($40\mu$m side) between LDD, GDD, and ISO at $T = 3 \times 10^4$ s (8 h, 20 min). The plotted values correspond to detail of panels A, B, and C of Figure S5.

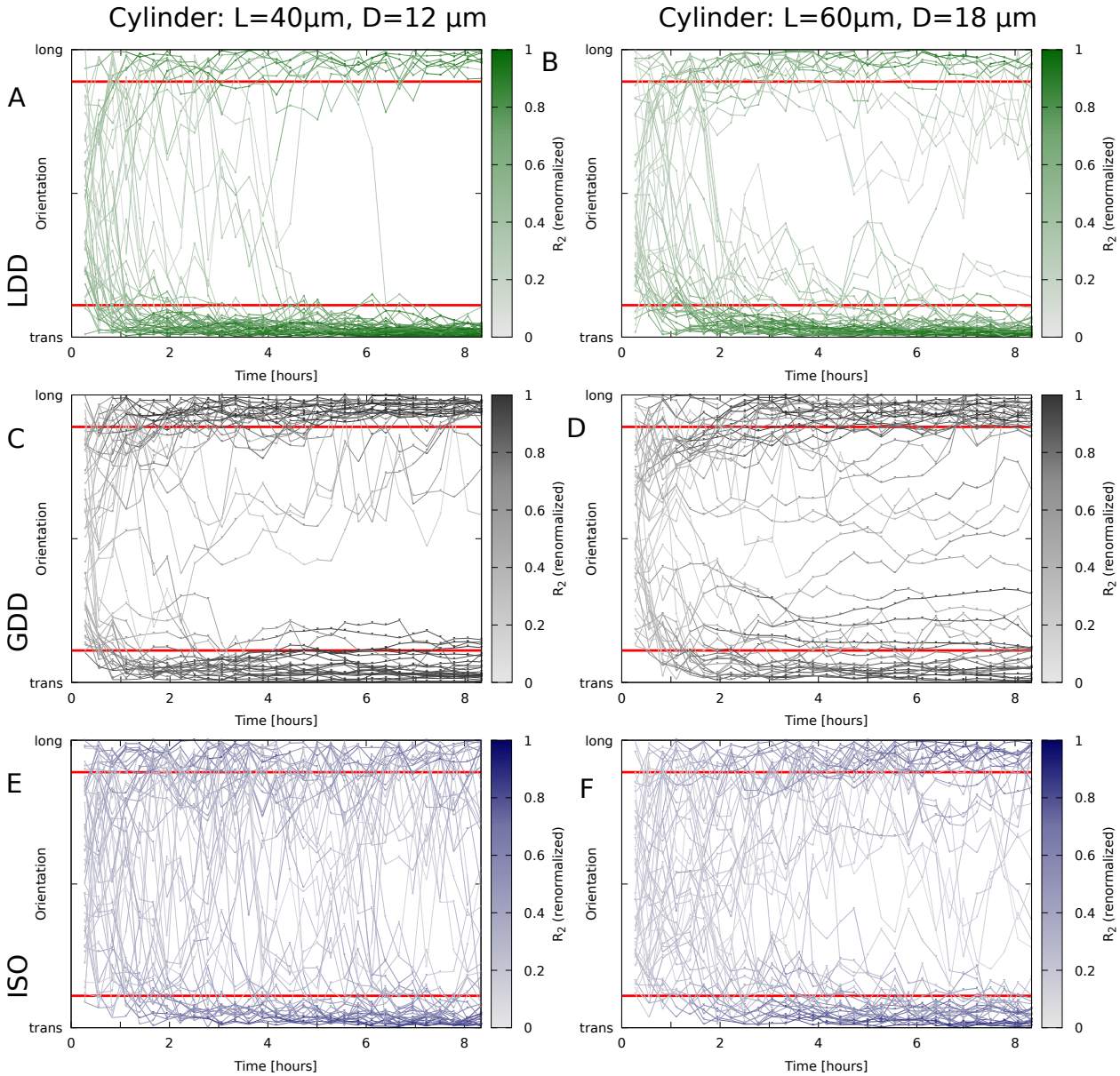


Figure S8: **Orientation over time with for individual simulations**. Lines depict the orientation of the array ($\Theta$ based on $R_2$) for n=50 simulations per nucleation mode / cylinder size. Lines are coloured by the degree of alignment, renormalized $R_2 = R_2/R_2(max|\Theta)$. Red lines indicate the boundaries of the "transverse" (trans) and "longitudinal" (long) categories in Figure 4. In most cases, $R_2$ increased substantially after the a stable orientation was obtained (near horizontal part of the traces). At the times of rapid reorientation, on the other hand, $R_2$ was relatively low. With both LDD microtubule-based (A,B) and isotropic (E,F) nucleation, the array orientation appeared more stable for transverse arrays than for longitudinal arrays, whereas for GDD microtubule-based nucleation (C,D), the stability looked more similar. Additionally, very few traces crossed the middle with GDD, whereas a full reorientation from longitudinal to transverse occurred in a substantial fraction of the runs with LDD and isotropic. Microtubule dynamic parameters were the same everywhere in the domain, regardless of orientation. Nucleation modes: LDD microtubule-based (A,B); GDD microtubule-based (C,D); isotropic (E,F). Cylinder sizes: length 40 $\mu$m, diameter 12 $\mu$m (A,C,E); length 60 $\mu$m, diameter 18 $\mu$m (B,D,F).

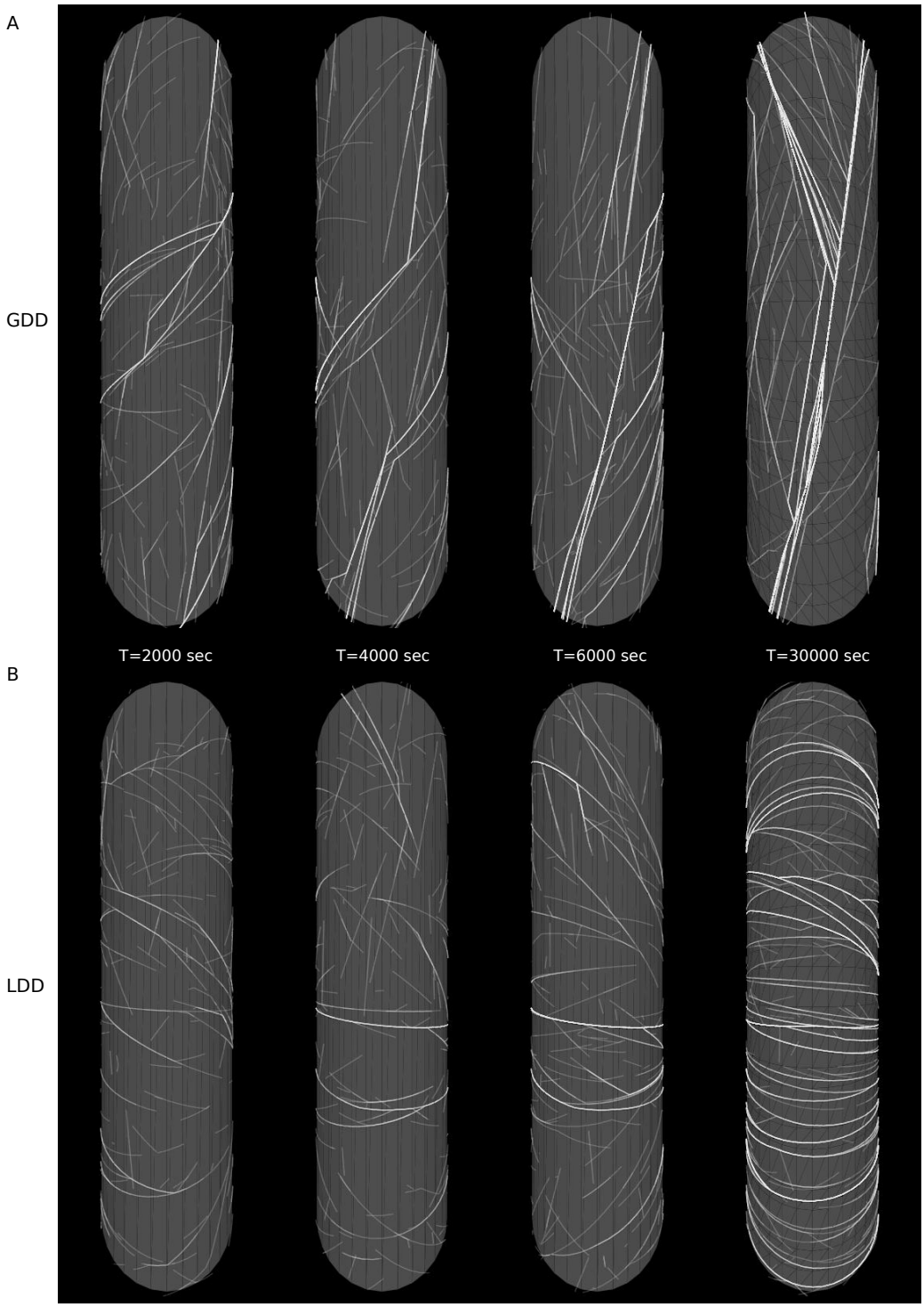


Figure S9: Snapshot of the simulated cortical array for (A) LDD and (B) GDD nucleation modes at four different time stamps. Simulation domain: cylinder with length= 40$\mu$m, diameter= 12$\mu$m. In these simulations: $r_c = 0.0025$ s$^{-1}$.

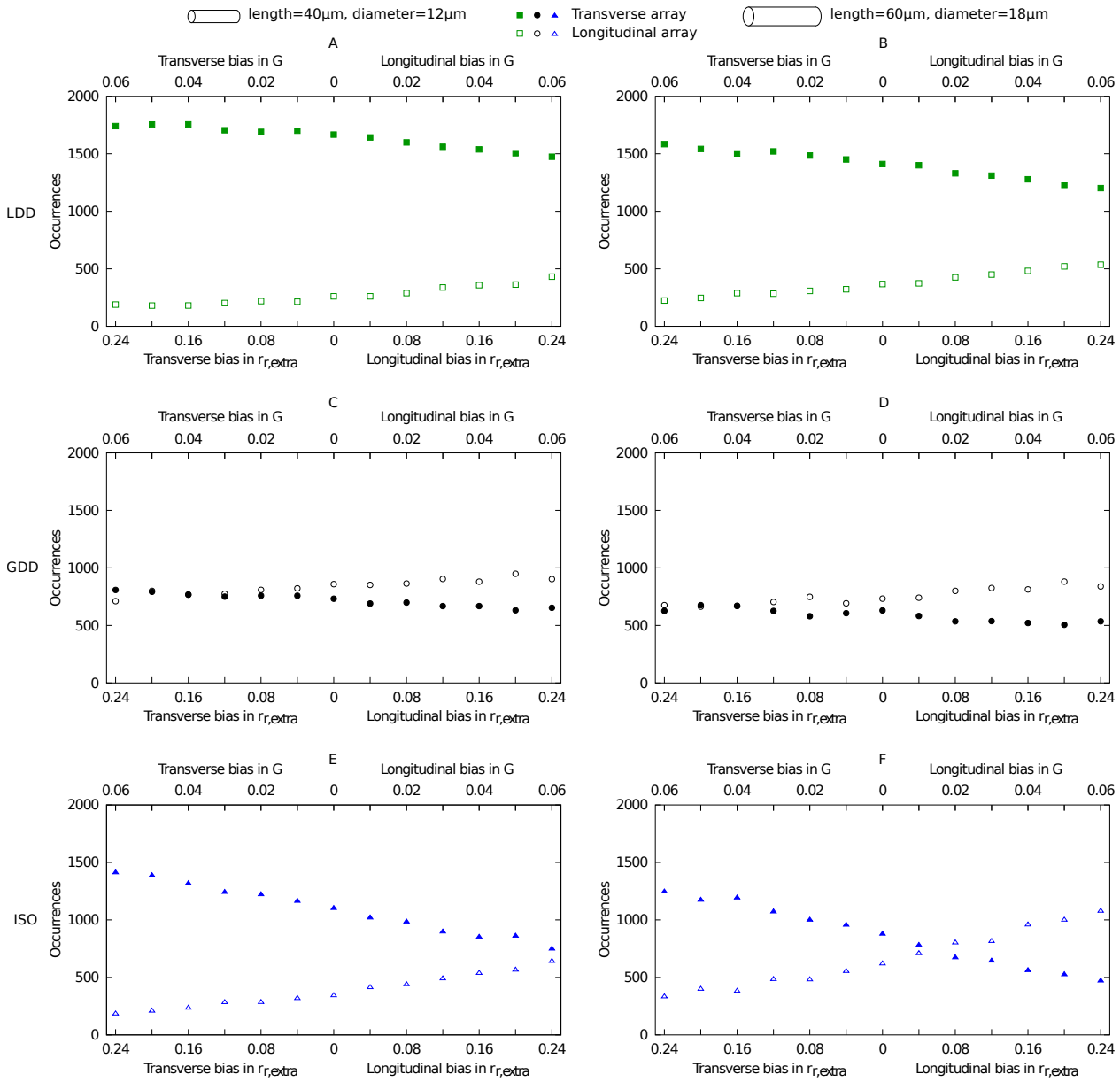


Figure S10: **LDD selects for more transverse arrays than GDD and ISO.** Number of aligned arrays at $T = 3 \times 10^4$ s (8 h, 20 min) with a transverse (filled symbols) or longitudinal (empty symbols) for the LDD (green squares), GDD (black circles), and ISO (blue triangles) cases, for different values of the longitudinal bias in $r_{r,\text{extra}}$ according to Equation (10). The simulation domain is a cylinder of (A) 40$\mu$m length and 12$\mu$m diameter, and (B) 60$\mu$m length and 18$\mu$m diameter. The upper horizontal axis translates the increased rescue rate into the maximum increase in $G$ in either the transverse or longitudinal directions. Error bars have been omitted because they are approximately the same size as the symbols. In these simulations, $r_c = 0.00225$ s$^{-1}$.